Pre-fusion AAA+ remodeling of target-SNARE protein complexes enables synaptic transmission

K. Ian White[1,2,3,4,5,**], Yousuf A. Khan[1,2,3,4,5], Kangqiang Qiu[6], Ashwin Balaji[7], Sergio Couoh-Cardel[1,2,3,4,5], Luis Esquivies[1,2,3,4,5], Richard A. Pfuetzner[1,2,3,4,5], Jiajie Diao[6], Axel T. Brunger[1,2,3,4,5,8,*]

[1]Department of Molecular and Cellular Physiology, Stanford University, Stanford, California, United States
[2]Department of Neurology and Neurological Sciences, Stanford University, Stanford, California, United States
[3]Department of Structural Biology, Stanford University, Stanford, California, United States
[4]Department of Photon Science, Stanford University, Stanford, California, United States
[5]Howard Hughes Medical Institute, Stanford University, Stanford, California, United States
[6]Department of Cancer Biology, University of Cincinnati College of Medicine, Cincinnati, United States
[7]Department of Chemistry, Stanford University, Stanford, California, United States
[8]Lead contact

[*]Correspondence: brunger@stanford.edu
[**]Correspondence: kiwhite@stanford.edu

Keywords

Membrane vesicle trafficking, AAA+ protein; neurotransmitter release; synapse; nanocluster; active zone; syntaxin; SNAP-25; NSF; ATP; hydrolysis

Summary

Membrane fusion is driven by SNARE complex formation across cellular contexts, including vesicle fusion during synaptic transmission. Multiple proteins organize trans-SNARE complex assembly and priming, leading to fusion. One target membrane SNARE, syntaxin, forms nanodomains at the active zone, and another, SNAP-25, enters non-fusogenic complexes with it. Here, we show that the AAA+ protein NSF (N-ethylmaleimide sensitive factor) and SNAP (soluble NSF attachment protein) must act prior to fusion. We show that syntaxin clusters are conserved, that NSF colocalizes with them, and characterize SNARE populations within and near these clusters using cryo-EM. Supercomplexes of NSF, α-SNAP, and either a syntaxin tetramer or two binary complexes of syntaxin—SNAP-25 reveal atomic details of SNARE processing and show how sequential ATP hydrolysis drives disassembly. These results suggest a functional role for syntaxin clusters as reservoirs and a corresponding role for NSF in syntaxin liberation and SNARE protein quality control preceding fusion.

40 # Introduction

41 The membrane-anchored SNARE (soluble N-ethylmaleimide-sensitive factor acceptor protein
42 receptor) proteins provide the energy to drive membrane fusion in various cellular contexts, such
43 as intracellular trafficking and exocytosis. One critical exocytic process is synaptic transmission,
44 in which a synaptic vesicle fuses with the presynaptic plasma membrane in the active zone of a
45 neuron to release neurotransmitter into the synaptic cleft in response to the arrival of Ca^{2+} in the
46 presynapse. While many proteins precisely act in concert to ensure synchronized and efficient
47 Ca^{2+}-triggered fusion[1–5], this process is fundamentally mediated by the "zippering" of four
48 SNARE motifs typically contributed by three to four SNARE proteins in the neuronal context—
49 syntaxin-1a and SNAP-25 on the target plasma membrane (*t*-SNAREs), and synaptobrevin-2 on
50 the vesicle (*v*-SNARE)—which come together to form a highly stable parallel four-helix bundle
51 during Ca^{2+}-triggered membrane fusion. This *cis*-SNARE complex must then be disassembled in
52 an ATP-dependent manner by the AAA+ protein NSF in concert with the adaptor SNAP
53 proteins[6,7].

54 While the molecular mechanisms of this core fusion cycle and the accessory proteins required to
55 ensure Ca^{2+}-dependent neurotransmitter release have been extensively studied[4], the organization
56 of the various components in the context of the crowded cellular milieu remains uncertain.
57 Numerous studies suggest nanoscale organization within the presynaptic active zone, where
58 proteins and lipids[8–11] such as cholesterol and PIP_2 colocalize or even phase separate into discrete
59 clusters with implications for organization within the active zone and even across the synapse[12].

60 The SNARE protein syntaxin shows such organization. Syntaxin is conserved from yeast to
61 mammals[13,14]; a short C-terminal transmembrane domain, a SNARE domain, and a C-terminal

62 Habc domain characterize it[15,16]. In the neuronal context, the majority (~ 67%) of syntaxin
63 molecules form nanodomains of non-uniform density[17,18], often near the active zone[8,17–21], and
64 these nanodomains frequently overlap with other essential active zone proteins and even docked
65 granules[19,20,22–25]. Morphologically, they are dense, around 50–60 nm in diameter, and harbor as
66 many as 70 syntaxin molecules each[17–19,22,26]. Increased presynaptic activity drives a decrease in
67 syntaxin cluster size[27]. These clusters depend on the syntaxin SNARE domain (H3), which
68 drives oligomerization[28].

69 Despite extensive study, the functional purpose of these clusters has remained unclear. Moreover,
70 NSF, α-SNAP, and syntaxin appear to interact *in vitro*[29], and α-SNAP associates with liposomes
71 presenting reconstituted full-length syntaxin[30]. Binary (syntaxin—SNAP-25) complexes of
72 different stoichiometries may also form [31–37], and NSF disassembles these complexes *in*
73 *vitro*[31,38–40]. Furthermore, continuous ATP hydrolysis by NSF on plasma-membrane mimicking
74 vesicles with reconstituted syntaxin and SNAP-25 produces a primed state for the most efficient
75 and synchronous synaptic vesicle fusion[3]. These observations support a critical role for NSF not
76 only in recycling SNARE proteins following fusion, but also in regulating the pool of fusogenic
77 syntaxin available to enter the vesicle fusion cycle.

78 Here, we show that spatially organized homo- or hetero-oligomers of syntaxin serve as
79 conserved molecular protein stores, and that NSF disassembles syntaxin nanodomains while
80 acting as a quality control factor to disassemble off-pathway binary complexes of syntaxin and
81 SNAP-25—a prerequisite for synaptic vesicle priming and fusion. We also describe the
82 molecular mechanism of disassembly and present a sequential ATP hydrolysis mechanism by
83 which NSF couples γ-phosphate release to SNARE substrate remodeling, with broad
84 implications for the AAA+ protein family.

85 # Results

86 ## Syntaxin nanodomains are conserved hotspots of NSF activity

87 First, we hypothesized that NSF is enriched at syntaxin clusters in the active zone, where it must
88 act to liberate fusogenic syntaxin molecules. To test this, we monitored the colocalization of
89 syntaxin and NSF in PC12 cells, a model system for neuronal secretion, using structured
90 illumination microscopy (SIM). All cells were transfected with GFP-syntaxin and as well NSF
91 with either a short C-terminal linker followed by mScarlet-I (NSF-mScarlet-I; Fig. 1A), a mutant
92 form of NSF (NSF(ΔN)-mScarlet-I; Fig. 1B,), or mScarlet-I alone (Fig. 1C). NSF-mScarlet-I is
93 hexameric and, together with α-SNAP, retains the capacity to bind and disassemble the ternary
94 SNARE complex (Fig. S1E). Clear, punctate co-clustering between NSF and syntaxin is visually
95 apparent upon inspection of the micrographs (Fig. 1A–C); Pearson's colocalization coefficient
96 (PCC) was calculated between the green and red channels to quantitate this (Fig. 1D, Methods).
97 Cells transfected with both GFP-syntaxin and NSF-mScarlet-I showed significant and
98 reproducible GFP-syntaxin-NSF-mScarlet-I colocalization (Fig. 1A, PCC = 60% ± 2%; $p <$
99 0.001 vs. mScarlet-I only;), suggesting an interaction between NSF and syntaxin molecules
100 within the nanodomains. As a control, mScarlet-I alone did not colocalize with syntaxin, showing
101 a nearly three-fold reduction in colocalization (Fig 1C; PCC = 22% ± 2%). To verify that
102 colocalization is consistent with the binding mode of NSF, in which NSF N-domains engage
103 multiple α-SNAPs, which in turn coat the SNARE complex[6,40,41], we examined colocalization of
104 GFP-syntaxin with a mutant form of NSF with the N-domain required for α-SNAP binding—and
105 thus SNARE complex binding—removed (NSF(ΔN)-mScarlet-I)[42]. As expected, this reduced
106 colocalization to a level nearly indistinguishable from the mScarlet-I control (Fig. 1B, PCC =
107 28% ± 3%; $p = 0.1776$ vs. mScarlet-I only). Two previously characterized[43] point mutations to

108 the D2 domain also disrupted colocalization between syntaxin and NSF (Fig. S1A–B). These
109 colocalization studies suggest that NSF associates with some multimeric species involving
110 syntaxin molecules *in vivo.* While these results showed clustering of syntaxin in the context of
111 synaptic transmission, we found that clustering also occurs in the case of the conserved syntaxin
112 homolog in yeast, Sso1p, as well (Fig 1F). During cell division, the mother cell transfers cargo to
113 the budding daughter cell via secretory vesicles; Sso1p clusters are enriched in the budding cell
114 in areas undergoing active fusion.

115 Discovery of a syntaxin tetramer complex with NSF—α-SNAP

116 To gain insight into the contents of the syntaxin nanodomains as well as the molecular basis of
117 the interaction between NSF and syntaxin, we purified the complex consisting of NSF, α-SNAP,
118 and soluble syntaxin (residues 2–253, transmembrane region omitted) by mixing the individual
119 purified proteins and performing size exclusion chromatography (SEC), Fig. S2A). We then
120 performed cryo-EM single-particle analysis (SPA) of this complex. Following 3D classification,
121 5% of the particles formed a class with an overall resolution of 3.75 Å, revealing a complex
122 (referred to as sx20S) between hexameric NSF, four α-SNAP molecules, and a parallel four-helix
123 bundle of syntaxin H3 SNARE domains (sx20S; Fig. 2A, Fig. S3, Tables S1–2). The remaining
124 particles showed no evidence of SNARE substrate. The existence of a syntaxin tetramer is
125 consistent with crosslinking mass spectrometry analysis of purified soluble syntaxin[36]. The
126 sx20S complex further supports the notion that NSF and α-SNAP recognize parallel, four-helix
127 SNARE complexes of variable composition[6,7].

128 Similar to structures of hexameric NSF and α-SNAP bound to the neuronal ternary SNARE
129 complex (referred to as 20S complex) under non-hydrolyzing conditions[6,41], the sx20S complex

130 forms a three-tiered architecture (Fig. 2A). NSF comprises three structured domains connected
131 by flexible linkers—the adaptor N-domain followed by the D1 and D2 AAA+ domains. Six NSF
132 protomers come together to form the active form of the enzyme, a homo-hexamer. In the top tier,
133 or spire, the NSF hexamer's multiple N domains bind four α-SNAP molecules and a tetramer of
134 syntaxin H3 SNARE domains. This spire structure positions the N-terminal end of the syntaxin
135 tetramer near the pore of the hexameric D1 ATPase ring of NSF; this middle tier is responsible
136 for ATP hydrolysis and SNARE complex disassembly. The bottom tier consists of the inactive
137 NSF D2 ATPase ring responsible for the oligomerization of the complex.

138 The spire structure is dynamic and rocks about relative to the D1 pore, but three of the six N
139 domains are relatively well-ordered and engaged with the α-SNAP—syntaxin sub-complex. The
140 D1 ring is asymmetric and split; protomers A–F are defined from the bottom of the split to the
141 top. All six D1 domains are ordered and engage the N-terminal linker preceding the H3 domain
142 of one of the four syntaxin molecules via conserved pore loops, which position Y294 such that it
143 intercalates between every other syntaxin substrate side chain passing through the pore (Fig. 2B).
144 The nucleotide states of the NSF ATPase domains are consistent with a pre-hydrolysis
145 conformation; D1 protomer A is ADP bound, while D1 protomers B–F are ATP bound with no
146 evidence for divalent cation as expected (Table S2). All D2 protomers are ATP bound and lack
147 divalent cation.

148 While the spire in the complete sx20S complex reconstruction was ordered enough to distinguish
149 the various components, continuous disorder limited the local resolution of the spire
150 reconstruction. To overcome this, we performed signal subtraction to remove the D1 and D2
151 rings, followed by local alignment of the α-SNAP—syntaxin sub-complex structure alone (Fig.
152 S3, Methods). This approach improved the resolution of the reconstruction of the α-SNAP—

153 syntaxin sub-complex to 4.25 Å, revealing a parallel, four-helix bundle of syntaxin SNARE
154 motifs with a density of sufficient quality to assign characteristic side chains (Fig. 2C). All four
155 helices are aligned in the same register, with a unique hydrophobic layer (-3 layer) composed of
156 four F216 side chains present; remarkably, all fit within the core of the bundle (Fig. 2D, Fig.
157 S9A) and induce little overall deformation of the individual H3 domains (Fig. S9B-D, bottom
158 row). The parallel syntaxin tetramer bundle observed in our structure would allow membrane
159 incorporation of the C-terminal transmembrane domains of all four syntaxin molecules (Fig. 2A).

160 To determine whether NSF and α-SNAP act to disassemble the syntaxin tetramer, we devised an
161 *in vitro*, gel-based disassembly assay (Fig. 1E). Wild-type NSF, α-SNAP, and soluble syntaxin
162 (residues 2–253) were purified independently, mixed in the absence of Mg^{2+} (*i.e.*, non-
163 hydrolyzing conditions), and the complex of all three was purified. The subsequent addition of
164 Mg^{2+} to the purified complex resulted in a significant loss of α-SNAP—syntaxin following
165 filtration relative to the non-hydrolyzing control, consistent with the disassembly of the syntaxin
166 tetramer and concurrent disassociation of α-SNAP (Fig. 1E, 21 ± 1% loss; Fig. S1D).

167 Structure of a 2:1 syntaxin—SNAP-25 complex with NSF—α-SNAP

168 In addition to the syntaxin homo-tetramer, hetero-oligomers with SNAP-25 are expected to be
169 present near or even within syntaxin nanodomains. Indeed, SNAP-25 colocalizes with syntaxin
170 in neurons[19,22,24] and readily forms binary complexes with syntaxin *in vitro*[31–35,44,45]. Although
171 SNAP-25 is required for fusion, assembly of a fusogenic ternary *trans*-SNARE complex likely
172 proceeds first through a syntaxin—synaptobrevin intermediate templated by Munc18-1, also
173 colocalized to syntaxin clusters[24], and by Munc13-1[31,46,47]. Disassembly of the binary complex is
174 critical, as genetic deletion of NSF is lethal[48]. However, an NSF mutation that differentially

175 blocks ternary, but not binary, SNARE complex disassembly causes only intermediate
176 sensorineural defects[38]. Thus, NSF and α-SNAP must first disassemble binary complexes of
177 syntaxin and SNAP-25 to set the stage for the action of Munc18 and Munc13, ultimately
178 resulting in synchronous and efficient Ca^{2+}-triggered fusion[3,31,32,46].

179 To gain insight into the structural nature of binary complex formation and disassembly by NSF,
180 we prepared a complex of NSF, α-SNAP, and the binary *t*-SNARE complex (21bin20S)
181 composed of full-length soluble SNAP-25 and soluble syntaxin-1a (1–267) in the absence of
182 divalent cation (*i.e.*, non-hydrolyzing conditions) and performed single-particle cryo-EM (Tables
183 S1–2, Fig. S2B, Figs. S4–5). First, models of the NSF D1 and D2 domains with substrate bound
184 in the D1 pore were built into two high-resolution (2.88 Å, 2.92 Å) classes from a single dataset,
185 differing only in the state of F protomer engagement with substrate (Fig. S4). Next, the dataset
186 from which they were derived was combined with two additional datasets to enable the 3D
187 reconstruction of weakly populated states with ordered density for the α-SNAP—SNARE spire
188 (Fig. S5). Classes with evidence of NSF D1 domains engaging ordered α-SNAP—SNARE sub-
189 complexes were carried forward; eight 21bin20S models were built into reconstructions ranging
190 from 3.39–4.01 Å in resolution, differing mainly in the orientation of N domains and a sub-
191 complex of three α-SNAP molecules and four SNARE motifs relative to the D1 ATPase ring
192 (Fig. S10A). All classes revealed substrate-bound NSF without Mg^{2+} needed for ATP hydrolysis
193 and disassembly (Table S2), and share the same overall architecture, with a spire composed of
194 NSF N-domains and the α-SNAP—SNARE subcomplex on top, the NSF D1 ring in the middle
195 tier, and the NSF D2 ring forming the bottom tier (Fig. 3A). In all cases, the NSF D1 ATPase
196 ring engages SNARE substrate, with one syntaxin molecule bound to the D1 ring pore in most
197 structures (Fig. 3B, Table S2).

198 Like the sx20S complex, continuous variability of the α-SNAP—SNARE subcomplex was
199 present in the 21bin20S reconstructions. We again performed signal subtraction and local
200 alignment on α-SNAP—SNARE sub-complexes from all five classes with ordered spire
201 structures (Fig. S5; see Methods). This procedure produced a single α-SNAP—SNARE sub-
202 complex reconstruction with an overall resolution of 3.74 Å (Fig. 3C), sufficient to assign
203 characteristic side chains, identify the SNAREs forming the complex and their directionality
204 (Fig. 3D, Fig. S9A). A model composed of the ternary neuronal SNARE complex[49] (PDB ID
205 1N7S) with synaptobrevin removed was docked into the density, preserving a distinctive kink in
206 the peptide linker leading into the SN2 SNARE motif of SNAP-25. In place of synaptobrevin, a
207 second syntaxin molecule was placed to complete the four-helix bundle with little deviation from
208 its usual backbone configuration of the ternary complex (Fig. S9B). As such, the stoichiometry
209 of the syntaxin—SNAP-25 complex observed is 2:1, the dominant species in solution[33,36,44,45].
210 Sidechains comprising essential layers repack within the core of the complex (Fig. 3D) compared
211 to the ternary SNARE complex. For example, the ionic central layer (0 layer) is reorganized;
212 Arg56 of synaptobrevin is replaced with a second Gln226 from the additional syntaxin molecule,
213 which adopts an extended rotamer to mimic the arginine it replaces. The SNAP-25 linker, which
214 joins the two SNARE motifs, is largely disordered but blocks binding by a fourth α-SNAP
215 molecule, as observed for the neuronal SNARE complex[6].

216 Docking the 2:1 binary complex structure back into the seven individual 21bin20S
217 reconstructions reveals an apparent preference for syntaxin, with six of eight reconstructions
218 featuring the N-terminus of syntaxin H3 bound within the pore of the D1 ring (Fig. 3B). As in the
219 case of the 20S with ternary SNARE complex, this observation is consistent with previous work,
220 in which disassembly was not contingent on specific SNARE N-terminus identity[6,40]. Taken

221 together, we observe that the NSF D1 ring can bind to at least two different SNAREs, syntaxin,
222 and SNAP-25, in various configurations.

223 Structure of a 2:2 syntaxin—SNAP-25 complex with NSF—α-SNAP

224 To gain insight into the disassembly of the binary SNARE complex, we repeated the binary 20S
225 preparation but added Mg^{2+} and an ATP regeneration system[50] (*i.e.*, hydrolyzing conditions) to
226 the purified complex ~1 min before vitrification for single particle cryo-EM (Tables S1–2, Fig.
227 S2C, Fig. S6). The addition of the regeneration system more closely mimics the metabolic state
228 of the cell, and it allows multiple cycles of SNARE disassembly and reassembly to proceed as
229 observed under far more dilute conditions[32]. Following 3D classification, 41% of particles
230 formed a complete complex, all of which have ordered α-SNAP—SNARE spire density and
231 differ largely by spire pose (Fig. S10A). Interestingly, classes with poorly defined SNARE
232 substrate, as observed under the non-hydrolyzing condition, were no longer observed. The
233 remaining 59% of particles were SNARE-substrate free and grouped into three classes with split
234 D1 and D2 rings; presumably, this is a post-disassembly, substrate-released state, and it is not
235 observed under non-hydrolyzing conditions.

236 Substrate-bound reconstructions reveal a flattened D1 ring in closer proximity to the D2 ring and
237 a strikingly different α-SNAP—SNARE spire structure than observed in the 21bin20S complex
238 under non-hydrolyzing conditions (Fig. 4A, Fig. S11A). Again, syntaxin is bound within the pore
239 of the D1 ring (Fig. 4B, Table S2). We observed a nearly symmetric α-SNAP—SNARE
240 subcomplex comprising four α-SNAP molecules coating a four-helix bundle. Even without
241 further processing, this structure was recognizable as a 2:2 syntaxin—SNAP-25 sub-complex
242 formed by two syntaxin H3 SNARE domains and two SNAP-25 SN1 SNARE domains; this

243 binary 2:2 configuration was previously observed in crystal structures of syntaxin-1 H3 and
244 SNAP-25 SN1 domains[34] and was unexpected as we prepared the complex with full-length
245 proteins, implying that two independent SNAP-25 molecules contribute their SN1 SNARE
246 domains to this complex. Presumably, disassembly of the binary 2:1 complex (Fig. 3C) had
247 occurred and was followed by reassembly to form the 2:2 binary complex (Fig. 4C) before
248 vitrification.

249 To improve the resolution of the spire reconstruction, signal subtraction, and local alignment
250 were performed as before (Fig. S6). This approach improved the reconstruction of the spire
251 proteins to 4.22 Å, enabling docking of a crystal structure of the 2:2 syntaxin—SNAP-25 SN1
252 complex[34] into the density (Fig. 4C), which was of sufficient quality to assign characteristic side
253 chains, to identify the SNARE domains and their directionality (Fig. 4D, Fig. S9A). The 2:2
254 binary complex was fit back into the full reconstructions, enabling modeling of the full
255 22bin20S. Furthermore, we were able to reproduce this result by reconstituting the complex with
256 only the SNARE domains of syntaxin and SNAP-25 under non-hydrolyzing conditions
257 (min22bin20S, Fig. S7A–D), yielding the same spire configuration but to a higher resolution of
258 3.86 Å following local reconstruction (Fig. S7E, Fig. S9A). This reconstruction also reveals the
259 interface between an N-domain of NSF and an α-SNAP molecule in detail; the interface is
260 characterized by a core hydrophobic interaction surrounded by charge complementation (Fig.
261 S7F).

262 Insights into SNARE substrate engagement and processing by NSF

263 Collectively, we obtained many datasets with NSF, α-SNAP, and several SNARE substrates
264 under non-hydrolyzing and hydrolyzing conditions (Tables S1–2), presenting an opportunity to

265 investigate the molecular mechanism of SNARE substrate processing and chemomechanical
266 energy transduction in NSF. Together, the resulting high-resolution structures derived from the
267 different classes from these datasets capture the hydrolysis cycle of NSF and reveal important
268 details about its reaction coordinate (Fig. 5–6, Figs. S11–13, Table S2).

269 For datasets with particles collected under non-hydrolyzing conditions, NSF is found in two
270 general conformations, primarily differentiated by their F protomer state (Fig. 5A, left column).
271 Two high-resolution 21bin20S classes from the 2:1 binary SNARE complex dataset reveal large-
272 scale conformational displacement connected to D1 F promoter nucleotide state and SNARE
273 substrate engagement. The first class is ATP-bound and fully SNARE substrate-engaged, while
274 the second has a nucleotide-free and SNARE substrate-disengaged F protomer (Fig 5A, left, top,
275 and bottom, respectively; Fig. S4). The engagement of F at the top of the ring accompanies a
276 relaxation of A into the split. Otherwise, the classes are nearly identical; protomers B–E D1
277 domains also bind ATP, while protomer A, at the bottom of the D1 split, is ADP-bound in both
278 cases. Comparison of the two classes reveals limited differences outside of the protomers A and
279 F positions, as the change in protomer F position allows additional relaxation of protomer A into
280 the split.

281 In contrast to the non-hydrolyzing datasets, particles in the hydrolyzing dataset fall into two
282 categories—substrate-bound 22bin20S (Fig. 5A, middle column) or substrate-free NSF (post-
283 hydrolysis; Fig. 5A, right column), of which there are ten and three classes, respectively (Table
284 S2, Fig. S6). The particles show a population shift towards a flatter D1 ring that is closer to D2
285 relative to the non-hydrolyzing class, particularly in the case of the SNARE-substrate free classes
286 (Fig. S11). Most strikingly, no SNARE substrate-bound classes show an F protomer as fully
287 engaged as those in non-hydrolyzing classes; in all but one class, F is ADP bound, SNARE

288 substrate disengaged, and sits between engaged A and E protomers. However, a subclass with an
289 ATP-bound F protomer was found using a subdivision of a large class with 3D Variability
290 Analysis[51] (3DVA; Fig. S6, Fig. 12C–D) for which the interprotomer interface with the
291 neighboring D1 protomer E is nearly—but not completely—formed. Critically, the pore loop
292 approaches the substrate-engaged state found in the non-hydrolyzing classes; together, this
293 reveals a trajectory of protomer A dissociation, nucleotide release and rebinding, and, finally,
294 SNARE substrate rebinding (Fig. 5D). Furthermore, classes with ordered syntaxin substrate are
295 gripped by the tyrosine residues in the pore of the D1 ring around eight residues further into the
296 primary sequence under hydrolyzing conditions (Fig. S10B).

297 Sequential hydrolysis by NSF drives conformational cycling

298 As noted above, the nucleotide states of the D1 protomers help explain the pattern of engagement
299 with the SNARE substrate (Fig. 5A–C, Table S2). How does nucleotide hydrolysis drive this
300 process? Unlike the non-hydrolyzing 21bin20S reconstructions, hydrolyzing 22bin20S
301 reconstructions are only ATP-bound in protomer E, indicative of a sequential hydrolysis
302 mechanism (Fig. 5A, middle column). Except for the rebinding F protomer described above, all
303 other D1 protomers are ADP bound with variability in the presence of Mg^{2+} and inorganic
304 phosphate (P_i); in most cases, protomers C and D have ADP•P_i and Mg^{2+}, protomer B is ADP-
305 bound, and protomer A is typically ADP-bound only. Finally, substrate-free classes are always
306 ADP bound, even in protomer E; they are flat, have some N-domains packed between the D1 and
307 D2 rings, and are characterized by a split in both the D1 and D2 rings between protomers A and
308 F (Fig. 5A, right column); this is consistent with a SNARE substrate side-loading mechanism
309 proposed for the NSF ortholog in yeast, Sec18[52]. In both hydrolyzing and non-hydrolyzing
310 datasets, all D2 domains are ATP-bound, with Mg^{2+} present in the hydrolyzing condition.

311 Together, these classes represent key steps in the hydrolysis cycle, revealing the binding of Mg^{2+},
312 hydrolysis of ATP to ADP•P_i at protomer E, and subsequent P_i release down-ring; these states are
313 accompanied by conformational change in the Walker A, Walker B, and Sensor 1 active site
314 residues in *cis* and the arginine fingers of the down-ring protomer in *trans* (Fig. 5B), and are
315 connected in turn to larger scale conformational change within the D1 domain (Fig. 5C).
316 Critically, P_i release following hydrolysis leads to arginine finger disengagement (Fig. 5B, right
317 two panels) and subsequent relaxation and solvation of the interprotomer interface, enabling the
318 protomer A transition to protomer F and subsequent substrate rebinding.

319 What triggers hydrolysis at E, and what conformational changes follow? While hydrolysis could
320 proceed spontaneously, this would be inefficient in the absence of an ATP-bound protomer F up-
321 ring to capture accompanying substrate translocation. We hypothesized that some allosteric
322 mechanism must regulate this process. To identify such a mechanism in an unbiased manner, we
323 performed principal components analysis (PCA) of Cα coordinates of 132 D1 protomers across
324 all datasets followed by hierarchical density-based clustering (HDBSCAN) in high-dimensional
325 space, revealing the conformational cycling of the NSF D1 protomers in a low-dimensional
326 coordinate as well as a corresponding allosteric mechanism for modulating hydrolysis by
327 protomers E (Fig. 6; see also Methods).

328 Overall, we find protomers divided into five interpretable clusters connected to ATP hydrolysis,
329 P_i release, and protomer cycling at the D1 split during SNARE disengagement, nucleotide
330 rebinding, and SNARE reengagement (Fig. 6A). Here, we focus on the unique features of the
331 protomers E under hydrolyzing conditions in two dimensions of the 11-dimensional latent space,
332 where they cluster far from other protomers (Fig. 6A, transition 1). As noted above, protomers E
333 are the only ATP-Mg^{2+} bound D1 protomers under hydrolyzing conditions (Fig. 6B), and they are

334 uniquely characterized by an extreme large-small subdomain angle (Fig. 6C, Fig. S11).
335 Examination of PCA and clustering results reveal conformational states unique to these
336 protomers (Fig. 6E), notably a discrete Walker A (α_3) helix position ("down" state) relative to the
337 rest of the D1 large subdomain that uniquely positions the nucleotide near key catalytic residues
338 (N374, R388; Fig. S13), a unique conformation of a highly conserved[56] segment of the N-D1
339 linker connected to N-domain engagement ("up A" state), and the absence of a fully engaged
340 "latch loop" (residues 457–467) contributed by the up-ring protomer F in *trans* ("intermediate A"
341 state; Fig. S12A). All three of these features appear structurally coupled (Fig. S12B) and
342 comprise an allosteric integration mechanism by which the position of nucleotide in the active
343 site is modulated at a distance by both N-domain engagement to SNARE substrate via the N-D1
344 linker conformation and by the presence of an up-ring protomer F via latch loop engagement.

345 To test the importance of the latch loop interaction in *trans*, a mutant form of NSF was generated
346 in which a portion of the latch loop (residues 460–466) is replaced with a short glycine-serine
347 linker (SGS). An NSF activity assay based on fluorescence dequenching (see Methods) shows a
348 highly significant, ~72% reduction in the rate of SNARE complex disassembly ($p = 0.0005$; Fig.
349 6D). On the other hand, the functional importance of the N-D1 linker has already been
350 established. We note that a mutation to NSF in the most conserved region N-D1 linker, I209N,
351 has a direct behavioral effect in zebrafish; NSF(I209N) is defective in the disassembly of ternary
352 SNARE complexes but not binary SNARE complexes, explaining this phenotype[38,56]. This
353 isoleucine side chain directly contacts the engaged latch loop and is adjacent to S207, a putative
354 phosphorylation site[53], raising the possibility of post-translational modification in regulating NSF
355 activity. Together, these observations support an allosteric mechanism critical in both effecting
356 and modulating NSF function.

357 # Discussion

358 Our observation of NSF colocalization to syntaxin clusters *in vivo*, coupled with direct structural
359 evidence of disassembly of both syntaxin tetramers and syntaxin—SNAP-25 complexes,
360 explains a previously overlooked but essential aspect of the synaptic vesicle fusion cycle, with
361 broad implications for membrane trafficking (Fig. 7A). While NSF is well known for its role in
362 ternary *trans*-SNARE complex disassembly following fusion, this work, combined with
363 functional studies[3,31,32,46], also establishes NSF as a critical factor for synaptic vesicle priming
364 before fusion. NSF is enriched at and near syntaxin clusters, which are, in turn, found at the
365 presynapse. The observation here of a parallel, four-helix syntaxin-1a bundle suggests that these
366 clusters must be structured, at least in part, and that NSF and α-SNAP act to disassemble the
367 syntaxin tetramers on the perimeter of a given cluster, increasing syntaxin mobility at the
368 synapse[27]. Individual syntaxin molecules liberated from clusters by NSF can then be captured by
369 the SM protein Munc18 and ultimately be used to assemble fusogenic *trans*-SNARE complexes.

370 However, a high local concentration of SNAP-25 is present near the syntaxin clusters as well, so
371 free syntaxin may also enter a non-productive binary SNARE complex with SNAP-25 with a
372 stoichiometry dependent upon local concentrations and configurations of either protein. In this
373 work, we observe binary complexes with two stoichiometries—2:1 and 2:2 binary complexes of
374 syntaxin and SNAP-25, with the latter re-forming following NSF-mediated disassembly of the
375 former under hydrolyzing conditions. The 2:1 configuration dominates in the non-hydrolyzing
376 condition—and in other *in vitro* studies[33,45]—but is derived from co-expressed proteins that were
377 extensively purified without NSF action. The 2:2 configuration is only found following NSF-
378 mediated disassembly of the 2:1 configuration. This effect may be due to the dissociation of the
379 SNAP-25 SN1 and SN2 domains during disassembly by NSF, increasing the likelihood of

380 binding to other SN1 domains in *trans*. The structural plasticity of the SNARE complexes is also
381 of note; taken together, the repeated observation of a twisted, parallel, four-helix bundle with
382 minimal backbone distortion (Fig S9B) emphasizes the functional conservation latent in the
383 SNARE domain sequences studied thus far, as well as the importance of additional SNARE
384 protein accessory domains in differentiating SNARE protein function[52].

385 Regardless, NSF and α-SNAP must thus constantly act to disassemble both syntaxin tetramers
386 and binary SNARE complexes to maintain a fusogenic population of *t*-SNAREs[3], which
387 ultimately enter the *trans*-SNARE complex with the *v*-SNARE synaptobrevin-2 and set the stage
388 for Ca^{2+}-triggered fusion in cooperation with synaptotagmin and complexin[54,55]. Indeed, the
389 energy released by SNARE protein zippering during vesicle fusion should be related to the
390 hydrolysis of ATP by NSF, which effectively maintains them in a high-energy state. Thus,
391 syntaxin nanodomains could effectively act as high-density storage sites for syntaxin, and NSF
392 could tap these stores under periods of high-frequency vesicle release. Modulation of NSF
393 activity by post-translational modification could thus be one way to regulate this process[38].
394 Finally, given the observation of clustered Sso1p in yeast, and the high degree of structural and
395 functional conservation between NSF and Sec18[52], this seems likely to be a conserved
396 organizing principle across fusion contexts.

397 At the atomic level, how does NSF accomplish the energy transfer needed to disassemble various
398 SNARE complexes? The structural details of the hydrolysis cycle (Fig. 5) suggest sequential
399 hydrolysis by the six D1 ATPase domains of NSF. Hydrolysis drives conformational change,
400 which is coupled to the application of force to one member of the SNARE complex, destabilizing
401 it and promoting disassembly (Fig. 7B, Movie S1). Rather than relying on a non-physiological
402 nucleotide state promoted by chelation of divalent cations or non-hydrolyzable nucleotide

403 analogs (*e.g.*, ATPγS), we established a reaction condition more closely approximating cellular
404 metabolism by using a physiological ATP regeneration system. Critically, hydrolysis proceeds
405 sequentially around the asymmetric NSF D1 ring, occurring near the "top" of the ring at
406 protomer E. Down-ring protomers reveal evidence for a transient post-hydrolysis reaction state
407 in which ADP•P_i is generally observed before P_i release from protomers C or B and an associated
408 disruption and solvation of the interprotomer interface. This mechanism is likely conserved in
409 other members of the AAA+ family, such as p97 (Supplemental Discussion).

410 Furthermore, the continuous transition from protomer A at the bottom of the ring to protomer F
411 at the top follows ADP release and ATP rebinding (Fig. 7B, Movie S1). This cycling appears
412 coupled to the triggering of hydrolysis at protomer E in a process allosterically mediated by
413 several key structural elements. Protomers E in the hydrolyzing condition position ATP in the
414 active site via a unique pre-hydrolysis conformation of the Walker A helix. Presumably, full
415 protomer F rebinding triggers hydrolysis, likely driven by an allosteric shift associated with full
416 latch engagement with the N-D1 linker region and further formation of the interprotomer
417 interface (Fig. 6, Fig. S12).

418 Protomer F rebinding is also connected to the mechanism by which engagement of the SNARE
419 substrate is maintained during processing. In the absence of a completely protomer F-rebound
420 state in the hydrolyzing condition, however, we cannot distinguish between SNARE substrate
421 rebinding before or after protomer E hydrolysis; the former case (ATP in fully rebound F and E)
422 represents a classical "hand-over-hand" mechanism, while the latter case (ATP in fully rebound
423 F, ATP ADP•Pi in E), a ratchet mechanism in which F re-engages substrate during or
424 immediately following a translocation event driven by protomer E hydrolysis, locking in any
425 substrate translocation that took place[57]. Given the highly flattened D1 ring state of the SNARE-

426 substrate free classes with ADP•Pi in protomers E (Fig. S11), the latter case is perhaps more
427 likely; flattening upon hydrolysis at protomer E could exert a pulling force on the substrate, and
428 translocation would then effectively take place with substrate engagement by a new protomer F
429 and release of the old protomer A.

430 Together, our findings expand the role of NSF in the membrane fusion cycle while further
431 demonstrating its contribution as a model system for understanding energy transduction and
432 protein remodeling in AAA+ proteins. NSF acts as a mobile engine of the presynapse—working
433 together with the SNAP adaptor proteins to convert the chemical energy latent in ATP into the
434 physical work needed to organize, maintain, and drive synaptic function through disassembly of
435 a variety of SNARE proteins.

436 Acknowledgments

437 We thank Richard Held, Jeremy Leitz, Rama Ranganathan, Subu Subramanian, Benjamin White,
438 Susan Wu, and Minglei Zhao for stimulating discussions; E. Montabana and C. Zhang for
439 assistance with the electron microscopy data collection at the Stanford University cEMc; and
440 Paul D. Adams, Pavel Afonine, and Nigel Moriarty for assistance with PHENIX refinement.
441 Funding was provided by the US National Institutes of Health (NIH; RO1MH63105 to A.T.B.)
442 and the Helen Hay Whitney Foundation/HHMI (to K.I.W.). Molecular graphics and analyses
443 performed with *UCSF ChimeraX*, developed by the Resource for Biocomputing, Visualization,
444 and Informatics at the University of California, San Francisco, with support from National
445 Institutes of Health R01-GM129325 and the Office of Cyber Infrastructure and Computational
446 Biology, National Institute of Allergy and Infectious Diseases. This article is subject to HHMI's
447 Open Access to Publications policy. HHMI laboratory heads have previously granted a non-

exclusive CC BY 4.0 license to the public and a sublicensable license to HHMI in their research articles. Pursuant to those licenses, the author-accepted manuscript of this article can be made freely available under a CC BY 4.0 license immediately upon publication.

Author contributions

K.I.W. and A.T.B. developed the research plan and experimental strategy. K.Q. and J.D. performed the cellular imaging experiments in PC12 cells and analyzed the data. Y.A.K. and A.B. performed the cellular imaging experiments in yeast and analyzed the data. K.I.W., Y.A.K. S.C., L.E., and R.P. purified all proteins. K.I.W., S.C., and Y.A.K. performed the disassembly experiments. K.I.W. performed the cryo-EM experiments and analyzed the data. K.I.W. and A.T.B. wrote the manuscript with input from the other authors.

Declaration of interests

All authors declare no competing interests.

Supplemental information

Associated Supplemental information file: Supplemental Discussion, Supplemental Figures 1–13 Supplemental Tables 1–2.

Supplemental Movie 1

Figures

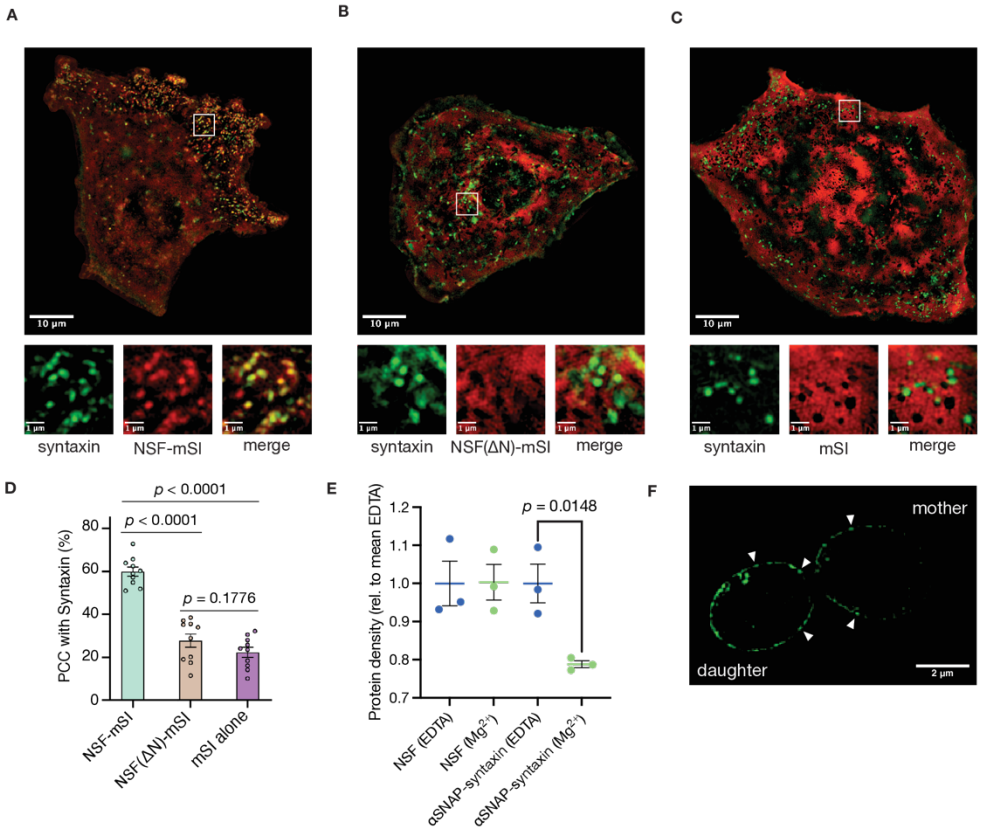

Figure 1 | NSF colocalizes to syntaxin nanodomains in an N-domain dependent manner and disassembles syntaxin oligomers

The interaction between NSF and syntaxin nanodomains in living cells. NSF-mScarlet-I and syntaxin-GFP were transfected into PC12 cells, and their conjugated fluorescent proteins were observed by SIM. Their interaction was assessed by measuring Pearson's colocalization coefficient (PCC) between the channels using *ImageJ*. Clustering of the syntaxin homolog Sso1p also occurs in yeast.

A. Colocalization between syntaxin-GFP nanodomains and wild-type NSF-mScarlet-I. NSF often forms punctate clusters that overlap with syntaxin (PCC = 60% ± 2%, mean ± SEM).

475 **B.** Colocalization between syntaxin-GFP nanodomains and NSF(ΔN)-mScarlet-I, in which the
476 N-domain of NSF that mediates the interaction with the α-SNAP—SNARE subcomplex has
477 been removed. Disruption of this interaction is evident and quantifiably reduces NSF
478 colocalization to syntaxin nanodomains (PCC = 28% ± 3%, mean ± SEM).

479 **C.** Control showing colocalization between syntaxin-GFP and mScarlet-I alone. No specific
480 interaction between these proteins is apparent (PCC = 22% ± 2%, mean ± SEM).

481 **D.** Comparison of wild-type NSF-mScarlet-I, NSF(ΔN)-mScarlet-I, and mScarlet-I clustering to
482 syntaxin-GFP nanodomains (M ± SEM, $n = 10$). Statistical significance was established by two-
483 tailed Student's *t*-tests, with $p < 0.05$ considered indicative of statistical significance.
484 Colocalization between wild-type NSF-mScarlet-I and syntaxin-GFP is significantly different
485 from both colocalization between NSF(ΔN)-mScarlet-I and syntaxin-GFP and colocalization
486 between mScarlet-I and syntaxin-GFP ($p < 0.0001$). Colocalization between NSF(ΔN)-mScarlet-
487 I and syntaxin-GFP and colocalization between mScarlet-I and syntaxin-GFP was not
488 significantly different ($p = 0.1776$).

489 **E.** NSF and α-SNAP disassemble oligomeric syntaxin as assessed by a gel-based de-enrichment
490 assay. sx20S was purified and split into two pools. EDTA was added to the first pool as a non-
491 hydrolyzing control, while Mg^{2+} was added to the second to initiate syntaxin complex
492 disassembly. Each pool was then concentrated using a 100,000 MWCO filtration device,
493 retaining 20S complex or α-SNAP—syntaxin subcomplex but allowing individual syntaxin and
494 α-SNAP molecules to pass, de-enriching them. Under hydrolyzing conditions, α-SNAP and
495 syntaxin were significantly de-enriched by around 21 ± 1% ($p = 0.0148$), consistent with the
496 disassembly of oligomeric syntaxin by NSF.

497 **F.** Sso1p forms dense clusters in the yeast plasma membrane during cell division (white
498 triangles). Sso1p-GFP was expressed in *S. cerevisiae* and imaged by SIM. Sso1p clusters were
499 enriched in the budding daughter cell (left); discrete clusters typically approached sizes near the
500 Nyquist limit of 160 nm (Fig S1C).

501

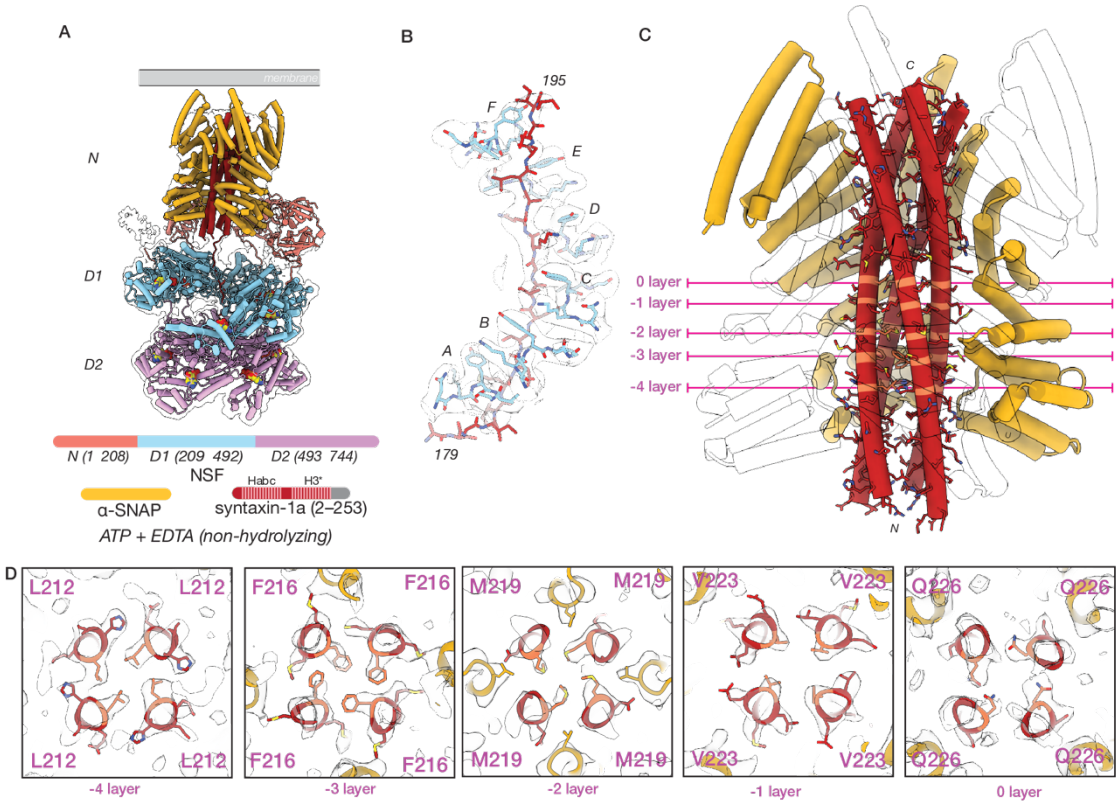

Figure 2 | NSF and α-SNAP engage a tetrameric SNARE complex composed of four syntaxin H3 domains

The structures of the sx20S (class #1, 3.75 Å) and the α-SNAP—syntaxin tetramer subcomplex (class #2, 4.07 Å).

A. Hexameric NSF engages the α-SNAP—syntaxin tetramer subcomplex via its N-domains (salmon), several of which engage four α-SNAP molecules (gold) surrounding the soluble, tetrameric syntaxin H3 complex (dark red) within the catalytic D1 ring of NSF (light blue). The structural D2 ring of NSF (purple) does not engage the SNARE substrate. A hypothetical membrane is illustrated in grey. For the SNARE proteins, domains visible in the reconstruction of the SNARE complex are indicated with an asterisk; the syntaxin Habc domains were not observed.

514 **B.** NSF engages one of the four syntaxin molecules in the tetramer via a series of pore loop
515 interactions; a tyrosine side chain (Y294) on each of the six protomers intercalates in between
516 every other side chain of a portion of syntaxin N-terminal to its H3 domain. The corresponding
517 sharpened map is contoured at 4 σ.

518 **C.** The α-SNAP—syntaxin tetramer subcomplex model, with two of the four α-SNAP models
519 hidden for clarity. The syntaxin H3 SNARE complex forms a twisted, parallel α-helical bundle
520 with a series of key SNARE complex layers preserved. See Fig. S9 for additional detail.

521 **D.** Slices through the α-SNAP—syntaxin tetramer subcomplex model and sharpened map at the -
522 4–0 layers, with key residues lightened for emphasis. Each layer is characterized by nearly planar
523 interactions between four identical side chains within the helical bundle. The primary
524 interactions between α-SNAP and the syntaxin H3 complex are observed near the -2 and -3
525 layers, where several functionally essential[58] α-SNAP side chains (L197, Y200) are positioned by
526 a loop that buries them within the groove of the bundle. No symmetry was imposed during
527 reconstruction.

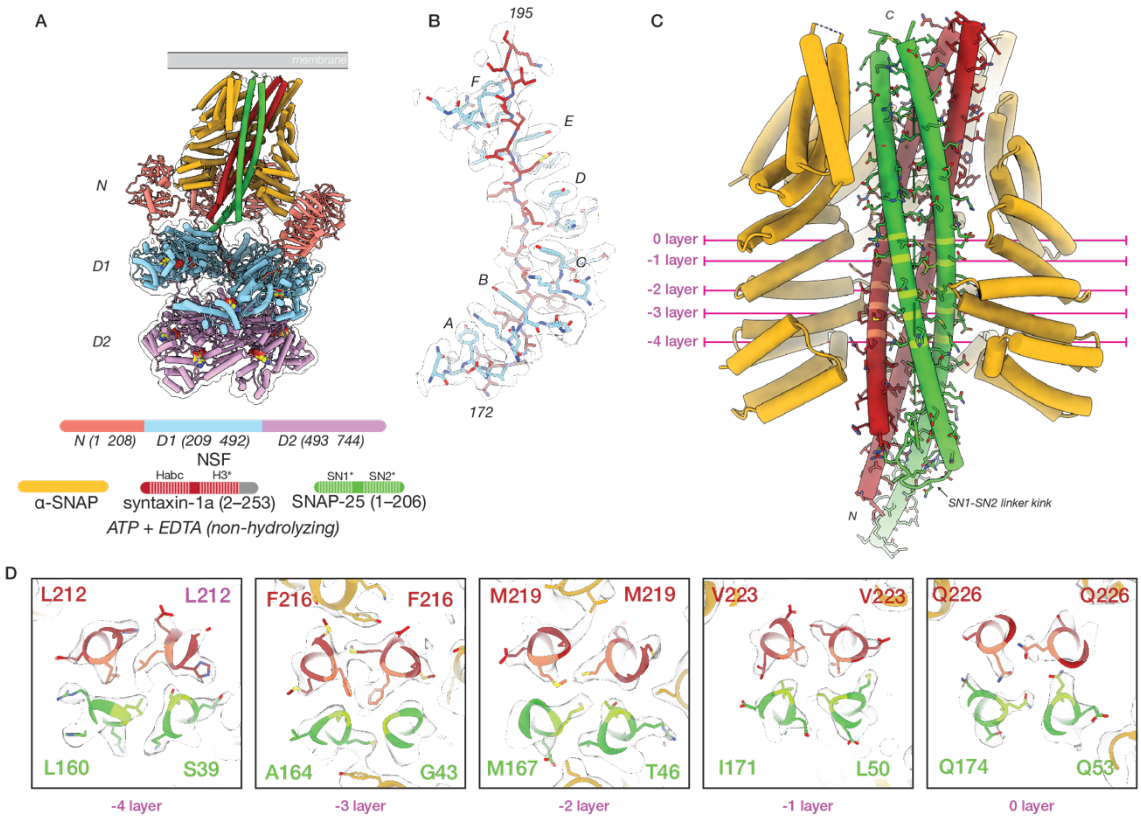

Figure 3 | NSF and α-SNAP engage a 2:1 binary SNARE complex of syntaxin H3 and SNAP-25 SN1 and SN2 SNARE domains under non-hydrolyzing conditions

A representative 21bin20S model (class #5, 3.39 Å) and the α-SNAP—2:1 binary SNARE subcomplex model (class #13, 3.74 Å).

A. Hexameric NSF engages the α-SNAP—2:1 binary SNARE subcomplex via multiple N-domains (salmon), which engage three α-SNAP molecules (gold) surrounding the 2:1 binary SNARE complex composed of two syntaxin H3 domains (dark red) and the SN1 and SN2 SNARE domains of a single SNAP-25 molecule (green). Part of the linker N-terminal to one of the syntaxin H3 domains is found within the catalytic D1 ring of NSF (light blue). The structural D2 ring of NSF (purple) does not engage the substrate. A hypothetical membrane is illustrated in grey. For the SNARE proteins, domains visible in the reconstruction of the SNARE complex are indicated with an asterisk.

541 **B.** NSF engages one of the two syntaxin molecules in the 2:1 binary SNARE complex via a
542 series of pore loop interactions involving Y294. A sharpened map is shown, contoured at 5 σ. Of
543 the eight 21bin20S classes with the 2:1 binary SNARE complex from the dataset collected under
544 non-hydrolyzing conditions, six have syntaxin molecules, and two have SNAP-25 molecules
545 bound to the pore of the D1 ring.

546 **C.** The α-SNAP—2:1 binary SNARE subcomplex model. Three α-SNAP molecules bind the 2:1
547 binary SNARE complex; a flexible linker between SNAP-25 SN1 and SN2 blocks access by a
548 fourth. The 2:1 binary SNARE complex forms a twisted, parallel α-helical bundle with a series
549 of characteristic SNARE complex layers preserved. This configuration also places the N-
550 terminal portion of the linker, which bears cysteines often palmitoylated *in vivo*, near the
551 membrane[59]. See Fig. S9 for additional detail.

552 **D.** Layer slices through the α-SNAP—2:1 binary SNARE subcomplex model and sharpened
553 map. Each layer is characterized by nearly planar interactions between four side chains within
554 the helical bundle. The primary interactions between α-SNAP and the syntaxin H3 complex are
555 found near the -2 and -3 layers, where several functionally essential[58] α-SNAP side chains (L197,
556 Y200) are positioned by a loop that buries them within the bundle groove.

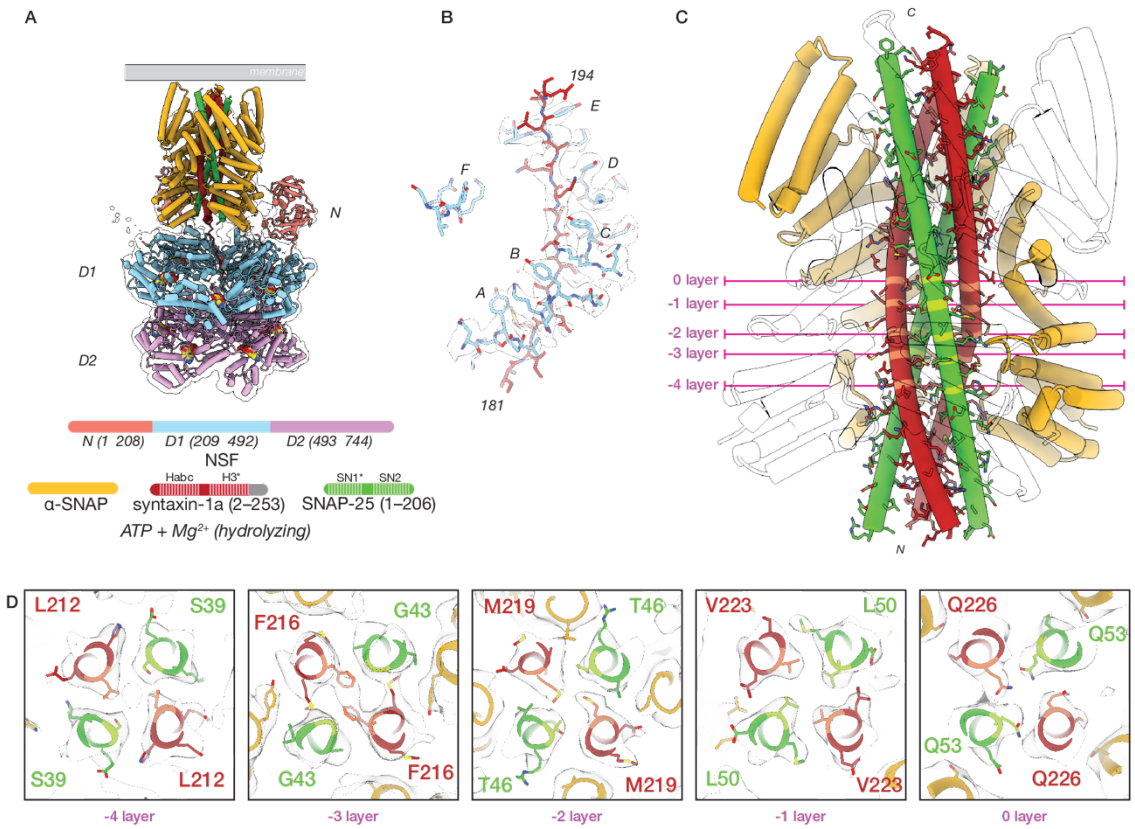

Figure 4 | NSF and α-SNAP engage a 2:2 binary SNARE complex of syntaxin H3 and SNAP-25 SN1 SNARE domains under hydrolyzing conditions

A representative 22bin20S model (class #19, 3.56 Å) and the α-SNAP—2:2 binary SNARE subcomplex model (class #23, 4.14 Å).

A. Hexameric NSF engages the α-SNAP—2:2 binary SNARE subcomplex via multiple N-domains (salmon), which engage three α-SNAP molecules (gold) surrounding the soluble, 2:2 binary SNARE complex composed of two syntaxin H3 domains (dark red) and two SNAP-25 SN1 domains contributed by two separate full-length SNAP-25 molecules (green). A portion of the linker N-terminal to one of the syntaxin H3 domains is observed within the catalytic D1 ring of NSF (light blue). The structural D2 ring of NSF (purple) does not contain density for a substrate. A hypothetical membrane is illustrated in grey. For the SNARE proteins, domains

visible in the reconstruction of the SNARE complex are indicated with an asterisk. See Fig. S9 for additional detail.

B. NSF engages one of the two syntaxin molecules in the 2:2 binary SNARE complex via a series of pore loop interactions involving Y294. A sharpened map is shown, contoured at 6 σ. Of the five 22bin20S classes with the 2:2 binary SNARE complex, all are found with syntaxin in the D1 pore, while two are observed with the N-terminus of the SNAP-25 SN1 domain in the pore.

C. The α-SNAP—2:2 binary SNARE subcomplex model. Four α-SNAP molecules bind the 2:2 binary SNARE complex, with two SNAP-25 SN1 SNARE domains and two syntaxin H3 domains. This configuration would place two independent N-terminal portions of the SNAP-25 linker bearing cysteine sidechains often palmitoylated *in vivo* near the membrane[59].

D. Slices through the α-SNAP—syntaxin tetramer subcomplex at the -4–0 layers. Each layer is characterized by nearly planar interactions between four side chains within the helical bundle. The primary interactions between α-SNAP and the syntaxin H3 complex are found near the -2 and -3 layers, where several functionally essential[58] hydrophobic α-SNAP side chains, L197 and Y200, are positioned by a loop that buries them within the bundle groove. Symmetry was not enforced during local reconstruction. Note that the near-twofold symmetry of the bundle leaves some sidechain densities poorly defined, likely resulting from the superposition of the syntaxin and SNAP-25 residues in a given layer.

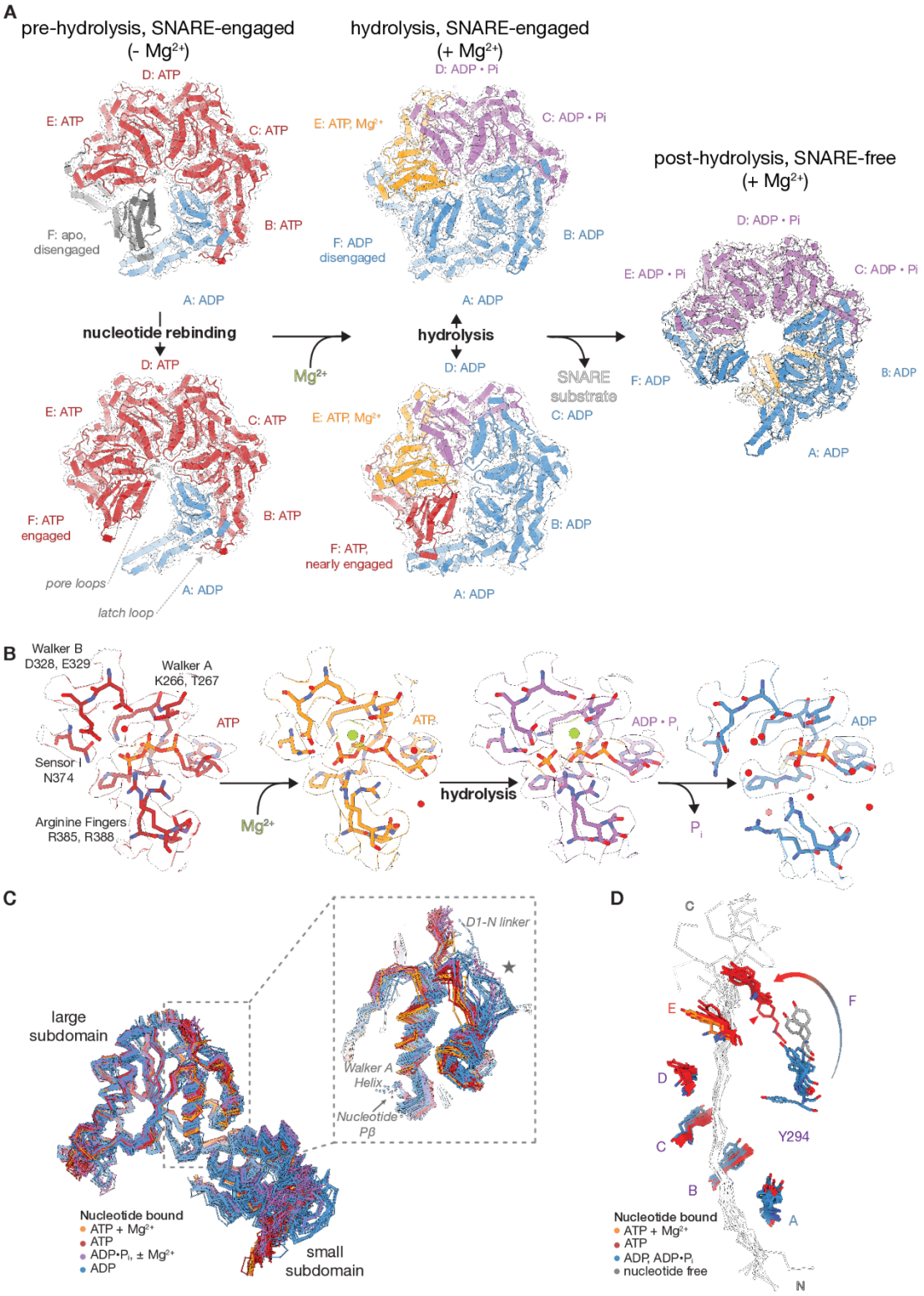

587

588 **Figure 5 | Comparison of NSF structures under non-hydrolyzing and hydrolyzing**
589 **conditions reveals interplay between sequential AAA+ hydrolysis and substrate rebinding**

590 **A.** Key conformational states of the NSF D1 ATPase ring. Two primary states dominate in the
591 absence of Mg^{2+} (left); the top class (#4) has a SNARE substrate disengaged, nucleotide-free
592 protomer F, while the bottom class (#3) has a fully SNARE substrate-engaged, ATP-bound F.
593 With the addition of Mg^{2+} (middle), E is ATP- and Mg^{2+}-bound. Protomers D, C, and
594 occasionally B retain P_i. and Mg^{2+}. All A protomers are ADP-bound. 3DVA-derived subclasses
595 reveal a coordinate for nucleotide exchange and protomer F engagement. The top subclass (#18)
596 has a substrate-disengaged, ADP-bound F. The bottom subclass (#17) has a nearly substrate-
597 engaged, ATP-bound F. Finally, substrate-free, post-hydrolysis classes such as #24 (right) show
598 an ATP-free D1 ring. For clarity, the spire, SNARE substrates, and the D2 ring are omitted in the
599 figures. See Tables S1–2 for more information on specific classes.

600 **B.** Atomic details of nucleotide hydrolysis. The P-loop binds nucleotide. Arginine fingers R385
601 and R388 from the down-ring protomer coordinate nucleotide phosphates. Without Mg^{2+}, a water
602 molecule sits between the nucleotide phosphates and Walker B residue side chains of D328 and
603 E329. Sensor 1 residue N374 is oriented towards the ɣ-phosphate of ATP. In the hydrolyzing
604 condition, Mg^{2+} appears in the active site, tightly coordinated by the β- and ɣ-phosphate moieties
605 of ATP and the side chain of Walker A motif T267. Following hydrolysis, ADP, P_i, and Mg^{2+}
606 remain; the side chains of Walker B residue E329 and Sensor 1 residue N374 tightly coordinate
607 the P_i as it disassociates. Subsequent P_i release down-ring leads to arginine finger disassociation,
608 disrupting the interprotomer interface. Active sites shown are derived (from left to right) from
609 D1 class protomers #4-E, #16-E, #16-D, and #16-B.

610 **C.** Alignment of 130 D1 protomers from 23 models derived from all four datasets. Structural
611 alignment was performed on the D1 large subdomains. Only Cα atoms of nucleotide-bound
612 protomers and corresponding Pβ atoms are shown for clarity. The inset (right) shows a key

613 region of the protein that shows changes in the N-D1 linker and N-terminus of the D1 domain
614 and the Walker A helix. The presence of the latch loop contributed by the up-ring protomer also
615 influences the conformational state of this region. In contrast, the loop is omitted for clarity, and
616 the binding location is indicated with a star.

617 **D.** Alignment of tyrosine residues in the pore of the D1 ring of substrate-bound models reveals
618 protomer F as the site of nucleotide exchange and substrate re-engagement. ADP-bound F is
619 disengaged from the substrate (blue). The release of ADP (nucleotide-free, grey) and ATP-
620 binding (red) are accompanied by a continuous transition to substrate engagement. The lowest
621 tyrosine corresponding to an ATP-bound F shown (red triangle) is from the 3DVA-derived model
622 shown in **A** (middle column, bottom).

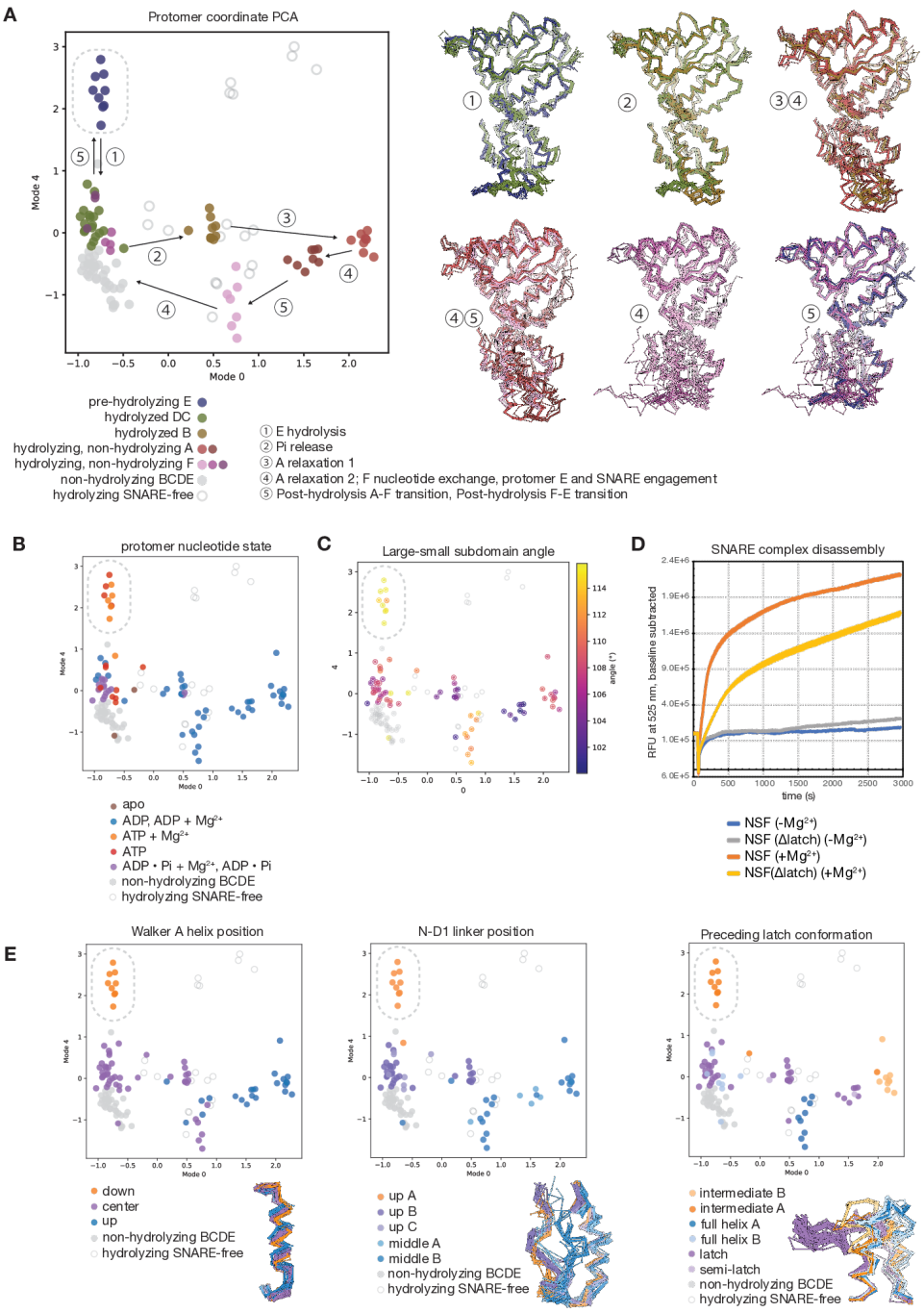

Figure 6 | Principal component analysis of NSF D1 protomer coordinates reveals further details related to sequential hydrolysis

A. 132 D1 domain models were aligned by large subdomain (residues 210–392), PCA was performed on Cα coordinates, and HDBSCAN was used to cluster the models in 11-dimensional space with a minimum cluster size of 3 models. Protomers cluster into discrete groups based on

629 conformation; these are easily distinguished upon projection into a 2D space defined by the first
630 and fifth modes. A proposed hydrolysis cycle connects these clusters as indicated by arrows
631 between clusters and descriptions below. Superimposed models corresponding to these
632 transitions are shown on the right. The cluster corresponding to pre-hydrolysis protomers E is
633 circled with a dashed line.

634 **B.** Protomer nucleotide state, mapped to the 2D PCA coordinate from **A**. The ATP + Mg^{2+} state is
635 unique to protomers E (top left, dashed line).

636 **C.** The angle (º) between helices α_3 and α_8 (a proxy for the relative angle between the D1 large
637 and small subdomains). Protomers E have the largest angle due (top left, dashed line).

638 **D.** A mutant form of NSF, NSF(Δlatch), was generated in which part of the latch loop (residues
639 460–466) was replaced with a short glycine-serine linker (SGS) and assayed for its ability to
640 disassemble the ternary SNARE complex composed of syntaxin, SNAP-25, and synaptobrevin,
641 relative to wild-type NSF as described previously[6]. Traces show the mean ± SEM of eight
642 replicates for each form of NSF, with and without adding $MgCl_2$ to initiate the reaction.
643 Disassembly rates were calculated by linear regression to each trace in the linear region of the
644 time course, from ~95–350 s, depending on the trace. NSF(Δlatch) disassembled SNARE
645 complex at 28 ± 1% the rate of wild type.

646 **E.** Three conformational features that distinguish the pre-hydrolysis protomer E cluster (top left,
647 dashed line), mapped to the 2D PCA coordinate from **A**. These features are in contact and
648 structurally coupled. The position of nucleotide in the active site is modulated by the position of
649 the Walker A helix (α_3), which occupies three discrete states; pre-hydrolysis protomers E occupy
650 the "down" state (left). The position of the helix is allosterically modulated by at least two

651 inputs. First, the N-D1 linker conformation (center) is connected to the state of N-domain
652 binding to α-SNAP, and it interacts with the latch loop of the up-ring protomer upon rebinding.
653 Second, the latch loop of the up-ring protomer contacts this region in *trans* and is also
654 structurally coupled (right). These two features push against the C-terminal end of the Walker A
655 helix and ultimately modulate the position of the ATP γ-phosphate relative to key catalytic
656 residues.

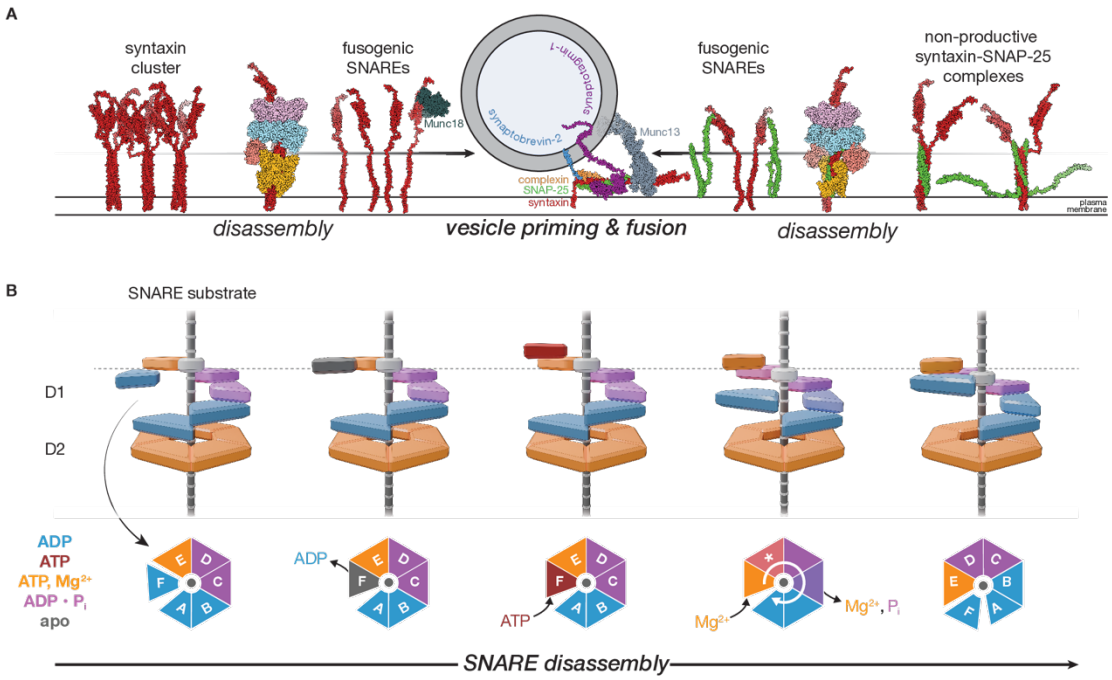

657

658 **Figure 7 | An expanded model for NSF action across cellular and atomic scales**

659 **A.** A model for disassembling non-fusogenic SNARE species by NSF and α-SNAP at the
660 presynapse and progression to priming and fusion. Syntaxin nanodomains comprised at least in
661 part of tetrameric syntaxin SNARE complexes serve as a reservoir for the liberation of
662 individual, fusogenic syntaxin molecules by NSF upon disassembly. These syntaxin molecules
663 may also enter non-productive binary complexes with SNAP-25, with 2:1 or 2:2 stoichiometry;
664 such complexes must also be disassembled by NSF to ensure *trans*-SNARE complex formation

665 with synaptobrevin on incoming synaptic vesicles in concert with other factors, such as Munc18,
666 Munc13, complexin, and synaptotagmin. Where possible, full-length structures (structures
667 reported here and PDB IDs 1N7S, 4JEU, 5W5C) were supplemented with AlphaFold2[60]
668 structures to provide additional context, and ISOLDE[61] was used with secondary structure
669 restraints to reposition flexible regions.

670 **B.** A sequential hydrolysis model for SNARE complex disassembly by NSF is inferred from
671 comparing different classes from non-hydrolyzing and hydrolyzing conditions. Following
672 hydrolysis-independent substrate side loading, the D1 ring is found in a pre-hydrolysis state with
673 ATP in protomer E of D1. Protomer F nucleotide exchange then enables ATP exchange and
674 rebinding to both SNARE substrate and the formation of the interprotomer interface with
675 protomer E, triggering ATP hydrolysis in protomer E and substrate translocation. This is
676 accompanied by P_i and Mg^{2+} release from down-ring protomers; in many structures, the release
677 occurs between protomers C and B. The cycle then begins anew. Blue corresponds to ADP-
678 bound, red to ATP-bound, purple to ADP•P_i bound, and grey to nucleotide-free. See Movie S1 for
679 an animated rendition.

680 # Methods

681 **PC12 transfection and imaging**

682 The PC12 cells, generously provided by Prof. Tobias Meyer from Stanford University, were
683 cultured on glass-bottomed dishes (MatTek; P35G-1.5-14-C) and allowed to adhere for 24 hr. To
684 introduce genetic material into the cells, transfection was performed using the TurboFect™
685 Transfection Reagent (#R0532, Thermo Fisher Scientific, USA) according to the manufacturer's
686 instructions. In brief, the plasmids (NSF-mScarlet-I plasmid: 1.75 μg; GFP-Syntaxin plasmid:

687 0.5 μg) were combined with 6.75 μL of TurboFect in 225 μL of DMEM medium (without FBS)
688 and incubated for 20 min. The DNA-TurboFect mixtures were carefully added drop-wise to the
689 cell cultures and incubated for 6 hr. Following the incubation, the cell cultures were replaced
690 with complete culture medium. After 24 hr post-transfection, the cells underwent three washes
691 with PBS. Subsequently, the cells were imaged using a structured illumination Nikon N-SIM
692 system (version AR5.11.00 64bit, Tokyo, Japan) equipped with an Apochromat 100×/1.49
693 numerical aperture oil-immersion objective lens. Using a 488 nm laser, the samples were excited
694 to acquire green SIM images, which captured emission within the 500–550 nm bandwidth,
695 specifically for GFP. Additionally, red SIM images were obtained by exciting the samples with a
696 561 nm laser to capture emission within the 570–640 nm bandwidth, corresponding to mScarlet-
697 I. To determine the degree of colocalization between syntaxin and NSF, Pearson's correlation
698 coefficient was calculated between channels *ImageJ*[62].

699 **Yeast imaging**

700 Super-resolution microscopy of *S. cerevisiae* expressing GFP-tagged Sso1 was performed using
701 structured illumination microscopy (SIM) on the OMX-Blaze system (Applied Precision,
702 Issaquah, WA). Glass-bottom dishes (1.5H, Cellvis) were pretreated with 0.01% poly-l-lysine by
703 adding 600–1000 μL to the center and incubated overnight. Following incubation, the dishes
704 were washed with deionized water to remove excess poly-l-lysine. Yeast cultures were grown
705 overnight, washed twice with phosphate-buffered saline (PBS), and resuspended to an optical
706 density (OD) of 0.4. A 10–20 μL volume of the yeast suspension was deposited onto the treated
707 dishes, followed by the addition of Diamond Antifade (Thermo Fisher Scientific) to prevent
708 photobleaching during imaging. The glass-bottom dishes were placed in a metal holder with 1–2
709 drops of immersion oil (refractive index 1.512) added before placement on the microscope stage.

710 SIM imaging was conducted using a laser appropriate for GFP excitation, and images were
711 captured with a 100× objective for a *z*-slice thickness of 0.125 µm, spanning a total thickness of
712 2.6 µm. Widefield images were also collected at 0.2 µm slice thickness when necessary.

713 **Protein expression and purification**

714 All NSF, the wild-type and mutant NSF-mScarlet-I, and NSF(Δ460–466) proteins were derived
715 from NSF from the Chinese hamster *C. griseus*, expressed in BL21(DE3)-RIL *E. coli*, and
716 purified as described previously[6], with final reassembly of hexameric NSF in reassembly buffer
717 (50 mM Tris pH 8.0, 150 mM NaCl, 1 mM EDTA, 1 mM ATP, and 1 mM TCEP). α-SNAP from
718 rat *R. norvegicus* was expressed in *E. coli* and purified as described previously[63]. Soluble rat
719 neuronal SNARE complex for the fluorescence-based disassembly assay (wild-type SNAP-25A,
720 syntaxin-1A 1–265, and 6×His-synaptobrevin-2 1–96) was purified by co-expression in C41 *E.*
721 *coli* and purified as described previously[63] Purified soluble rat neuronal SNARE complex was
722 fluorescently labeled with Oregon Green 488 maleimide dye as described previously[6].

723 Syntaxin-1A fragment 2-253 (Stx^{2-253}) was N-terminal His_6-tagged using the plasmid pTEV5.
724 Overexpression in *E. coli* BL21(DE3) was carried out in 8 L of auto-inducible media at 37ºC for
725 4 hr and then 30ºC overnight. Cells were collected by centrifugation; half of the pellet was
726 resuspended into 200 mL of 50 mM TRIS pH 8, 500 mM NaCl, and 10 mM imidazole and
727 supplemented with DNAse, lysozyme, 1 mM $MgCl_2$, and 2 eComplete Protease Inhibitor
728 Cocktail tablets (Roche). Cells were lysed by sonication (1 s on/3 s off, total 20 min, 55%
729 amplitude, 4ºC). Debris were removed by centrifugation at 43,000 rpm for 30 min at 4ºC using a
730 Ti45 rotor. The supernatant was then mixed with 5 mL of nickel-NTA agarose resin (Qiagen)
731 equilibrated with the lysis buffer. The suspension was gently stirred for 1 hr at 4ºC. The resin was
732 subsequently recovered by centrifugation at 4,200 rpm for 10 min at 4ºC, poured into a column,

733 and attached to an AKTA Start (Cytiva). An extensive wash was performed using 20 CV of 50
734 mM TRIS pH 8, 500 mM NaCl, and 40 mM imidazole until the 280 nm signal was stable.
735 Protein was eluted in 1 mL fractions in 50 mM TRIS pH8, 200 mM NaCl, and 400 mM
736 imidazole. Syntaxin-enriched fractions were identified by SDS-PAGE and pooled. To remove the
737 His-tag, the protein was mixed with an excess of TEV protease and dialyzed against 20 mM
738 HEPES pH 7.5, 50 mM NaCl, 1 mM DTT, overnight at 4ºC. The sample was centrifuged at
739 4,000 rpm for 10 min at 4ºC, filtered, and loaded onto a Mono-Q 5/50 column attached to an
740 AKTA Pure (Cytiva). The resin was extensively washed with 20 mM HEPES pH 7.5, 50 mM
741 NaCl, 0.2 mM EDTA until 280 nm signal was stable. Elution was performed in 120 CV over 2 hr
742 from 0.050–1 M NaCl. 2 mL fractions within the major peaks were run on SDS-PAGE, and
743 fractions containing Stx^{2-253} were concentrated using a 10 kDa cutoff centrifugal filtration device.
744 The concentrate was filtered and further purified using a Superdex Increase 75 16/60 column
745 (Cytiva) equilibrated with 20 mM TRIS pH 8, 150 mM NaCl. Fractions were run on an SDS-
746 PAGE, and fractions containing Stx^{2-253} were concentrated using a 10 kDa MWCO centrifugal
747 filtration device. A final concentration of 745 mM was determined by using the extinction
748 coefficient 5,960 M^{-1} cm^{-1}. Stx^{2-253} was aliquoted, flash frozen, and stored at -80ºC until further
749 use. An independent sample purified from the same batch of cells was analyzed on MALDI-TOF,
750 and a monomeric molecular weight of 29,208.50 g/mol was confirmed.

751 Binary neuronal SNARE complex for cryo-EM imaging studies (SNAP-25A with all cysteines
752 mutated to serine, syntaxin-1A 1–267) was purified following co-expression of SNARE proteins
753 from *E. coli* BL21 STAR (Invitrogen). Cells were grown overnight at 30°C using an auto-
754 inducing LB medium[64]. After harvesting the cells by centrifugation, the pellet was resuspended
755 in lysis buffer (50 mM NaPi pH 8.0, 300 mM NaCl, 20 mM imidazole, 0.5 mM TCEP)

756 supplemented with lysozyme, DNase I, and antiprotease tablets (Roche) and subjected to
757 sonication (3 s on, 9 s off, 60% power for 5 min, repeated 3×) and centrifugation (10,000 rpm for
758 10 min followed by 43,000 rpm for 40 min). The clarified lysate was bound to Ni-
759 NTA agarose beads (QIAGEN) equilibrated in a lysis buffer. Beads were harvested by
760 centrifugation (2200 rpm for 10 min), poured into a gravity column, and washed with lysis
761 buffer, urea buffer (50 mM NaP_i pH 8.0, 300 mM NaCl, 30 mM imidazole, 0.5 mM TCEP, 7.5 M
762 urea), and wash buffer (50 mM NaPi pH 8.0, 300 mM NaCl, 30 mM imidazole, 0.5 mM TCEP).
763 The SNARE complex was then eluted with wash buffer supplemented with an additional
764 320 mM imidazole. The fresh eluent of the Ni-NTA affinity purified SNARE complex was
765 supplemented with tobacco etch virus (TEV) protease and dialyzed against buffer A1 (50 mM
766 Tris-HCl, pH 8.0, 250 mM NaCl, 0.5mM TCEP) overnight at 4°C. After dialysis, the sample was
767 diluted to a final NaCl concentration of 50 mM using buffer A1 without NaCl, and the His-tag-
768 free complex was subjected to anion exchange chromatography (Buffer A2: 50 mM Tris-HCl, pH
769 8.0, 50 mM NaCl, 0.5 mM TCEP; Buffer B1: 50 mM Tris-HCl, pH 8.0, 500 mM NaCl, 0.5 mM
770 TCEP) using a MonoQ 4.6/100 column (Cytiva) and a linear gradient of NaCl starting at 50 mM
771 and ending at 500 mM. The peaks containing the purified complex were pooled and loaded onto
772 a Superdex 75 16/60 column to normalize NaCl concentration (50 mM Tris-HCl pH 8.0, 50 mM
773 NaCl, 0.5 mM TCEP).

774 The sx20S supercomplex was formed by mixing ATP-bound NSF, α-SNAP, and syntaxin to a
775 ratio of 1:5:30 in reassembly buffer and purifying it by size-exclusion chromatography using a
776 Superose 6 10/300 GL column; the first peak to elute was collected and concentrated to around
777 15 mg mL^{-1} for vitrification and cryo-EM imaging. The 21bin20S supercomplex was purified
778 similarly but with a 1:5:30 ratio of NSF:binary SNARE complex:α-SNAP. In the case of

779 preparing 21bin20S supercomplex for imaging under hydrolyzing conditions, EDTA was omitted
780 from the final SEC buffer.

781 **Gel-based syntaxin disassembly assay**

782 Soluble syntaxin (2–253) and α-SNAP were mixed at concentrations of 100 μM and 150 μM,
783 respectively, in 50 mM Tris pH 8.0, 150 mM NaCl, 1 mM TCEP, and 1 mM EDTA (SEC buffer)
784 and incubated for 20 min. NSF was subsequently added to a final concentration of 2.5 μM,
785 bringing the total reaction volume to 500 μL. The mixture was then injected into a Superdex 200
786 16/60 column (Cytiva) and complex peak fractions were pooled and concentrated using a
787 100,000 MWCO filtration device. For each assay condition, 5 μg of complex was used. Two
788 experimental conditions were performed in triplicate; either EDTA or $MgCl_2$ was added to a final
789 concentration of 4 mM. Samples were incubated for 20 min at room temperature and re-
790 concentrated using 100k MWCO filters before SDS-PAGE. Re-concentration effectively de-
791 enriches liberated syntaxin and α-SNAP molecules. Densitometry was performed using
792 *ImageJ*[62], and statistical significance was established between the conditions using a two-tailed
793 Student's *t*-test.

794 **Gel-based ternary SNARE complex disassembly assay**

795 To verify that NSF activity was not hampered by the C-terminal addition of mScarlet-I, SNARE
796 complex disassembly was evaluated by gel electrophoresis. NSF, NSF-mScarlet-I, α-SNAP, and
797 the neuronal SNARE complex were dialyzed into 25 mM TRIS pH 8, 150 mM NaCl, 1 mM ATP.
798 Then, components were combined into either EDTA buffer (25 mM TRIS pH 8, 2 mM ATP, 1
799 mM EDTA) or Mg^{2+} buffer (25 mM TRIS pH 8, 2 mM ATP, 4 mM $MgCl_2$). The reaction volume
800 was 10 μL, and contained 500 nM NSF or NSF-mScarlet-I and 50 nM α-SNAP. Assays were
801 started by adding 10 μM SNARE complex, and samples were then incubated at 37ºC for 10 min

802 in a thermocycler. 2 uL of 5×-Laemli loading buffer was then added, and samples were
803 incubated at 95ºC for 5 min. Finally, 5 µL of each reaction was loaded onto an AnykD TGX gel
804 (BioRad) and run at 200 V for 45 min. The gel was stained with Coomassie R-250 (BioRad). As
805 internal controls, all single components were diluted at a similar concentration as the reactions
806 using Mg^{2+} buffer and treated in parallel. Note that the additional control marked as "SNARE
807 complex unboiled" corresponds to the SNARE complex incubated at 37ºC but not at 95ºC after
808 adding loading buffer. For reference, monomeric NSF is ~83 kDa while NSF-mScarlet-I is ~112
809 kDa.

810 **Fluorescence dequenching-based neuronal SNARE complex disassembly assay**

811 The details of the fluorescence dequenching assay have been previously described[6,32,38,40,41,63].
812 Fluorescence dequenching assays were carried out using a FlexStation II 384-well plate reader
813 (Molecular Devices) with a final reaction volume of 60 µL in 20 mM Tris pH 8, 100 mM NaCl, 2
814 mM ATP, and 0.5 mM TCEP. The assay plate was first prepared by adding 50 µL of 60 nM wild-
815 type or Δ460–466 mutant NSF, 2.4 µM α-SNAP, 480 nM OG-labeled neuronal SNARE complex
816 in reaction buffer to each well. Then, 100 µL of reaction buffer (as a control) or ATP hydrolysis
817 initiation buffer (reaction buffer supplemented with 24 µM $MgCl_2$) was added to appropriate
818 wells of the compound plate, and fluorescence dequenching was monitored. Excitation was
819 performed at 485 nm, and emission was monitored at 525 nm with a dichroic mirror at 515 nm.
820 First, fluorescence intensity was monitored before reaction initiation for 60 s. Then, 10 µL of
821 compound plate solution was transferred to each assay plate well (diluting all protein 5/6-fold
822 and $MgCl_2$ concentrations six-fold) and triturated, initiating the disassembly reaction. The final
823 protein concentrations following mixing were 50 nM NSF, 2.0 µM α-SNAP, and 400 nM
824 SNARE complex. The final $MgCl_2$ concentration was 4 mM. Dequenching was then monitored

825 for 30 min at 20 ºC. Linear regression over the first several minutes was performed to estimate
826 relative disassembly rates. The statistical significance of changes to disassembly rates was
827 assessed using the two-tailed Student's *t*-test.

828 **Sample vitrification for cryo-EM SPA**

829 The samples were prepared immediately before vitrification (Fig. S2). Quantifoil R1.2/1.3 200
830 mesh gold grids (Quantifoil Micro Tools GmbH, Germany) were cleaned with chloroform, dried
831 for several hours, and subjected to glow discharge using a PELCO easiGlow Glow Discharge
832 Cleaning System (Ted Pella) under vacuum at 15 mA for 45 s with a 15 s hold time. Immediately
833 following 21bin20S or sx20S supercomplex purification, proteins were concentrated to ~15 mg
834 mL^{-1} in 17 µL. For the hydrolyzing condition, 2 µL of 10 × ATP Regeneration Solution (50 mM
835 Tris pH 8.0, 150 mM NaCl, 1 mM ATP, 160 mM creatine phosphate, and 0.3 mg/mL rabbit
836 muscle creatine kinase (Roche)) was added, and the sample was incubated on ice for 2 min; in
837 contrast, 2 µL of reassembly buffer was added in the case of non-hydrolyzing conditions. Then,
838 for the hydrolyzing condition, 1 µL of 20 × Reaction Initiation Solution (50 mM Tris pH 8.0, 150
839 mM NaCl, 1 mM ATP, 20 mM MgCl2, 1% Nonidet P-40) was added, otherwise 1 µL of 1%
840 Nonidet P-40 was added in the case of non-hydrolyzing conditions. Using a Vitrobot Mark IV
841 (Thermo Fisher Scientific), 4 µL of a given sample was applied to a grid at room temperature
842 and 100% humidity and, blotted for 4 s with a blot force of 3, and subsequently plunge-frozen in
843 liquid ethane.

844 **Cryo-EM SPA data collection**

845 Grids were imaged using a Titan Krios electron microscope (Thermo Fisher Scientific) operated
846 at 300 kV and equipped with a K3 camera (Gatan). Data collection was performed using
847 *SerialEM*[65]. All datasets were collected with a nominal magnification of 22,500× for a physical

848 pixel size of 1.096 Å and a super-resolution pixel size of 0.548 Å. Dose rate was either ~10 or
849 ~20 e^-/px/s depending on whether correlated double sampling (CDS) was enabled on the K3, for
850 a total dose of around 30 $e^-/Å^2$. Nine grid holes were imaged for each stage movement using
851 multiple record setup in *SerialEM*, with one collection per hole. At each hole, either a 2 s or 4 s
852 exposure fractionated into either 40 or 80 frames was collected, depending on whether CDS was
853 enabled. Defocus values ranged from -1–-3 µm. See Table S1 for details.

854 **Cryo-EM SPA image processing**

855 All cryo-EM datasets were processed using a software pipeline consisting of *MotionCorr2*[66],
856 *CTFFIND4*[67], *RELION 3*[68,69], and *cryoSPARC*[51,70]. Early-stage processing was carried out in
857 *RELION 3*, with final 3D refinement and variability analysis carried out with *CryoSPARC*.
858 Dataset-specific processing schemes are presented in Figs. S3–7. Generally, all processing
859 proceeded as follows. Processing began in *RELION 3*, with per-micrograph optics groups
860 defined for a given dataset based on the nine beam shift positions using the custom script
861 *update_relion_tilt_class_og.py*. For example, the hydrolyzing condition micrographs were
862 collected in two sessions, so 18 total optics groups were defined. The raw image stacks were
863 dose-weighted and motion-corrected using the *RELION* implementation of *MotionCorr2*, with
864 seven patches along the *x* direction and five patches along *y*. CTF parameters were estimated for
865 each micrograph using *CTFFIND4* with a resolution range of 3–30 Å, an FFT box size of 1024
866 px, and otherwise default parameters. Micrographs were then selected based on maximum
867 resolution and the CTF figure of merit.

868 Generally, an initial round of manual picking, extraction, and 2D classification were used to
869 assess data set quality and provide particles to reconstruct an initial 3D model. Good particles
870 from manual picking were then used for automated particle picking in *RELION*. Particles were

871 then extracted with a box size of 640 px, binned 8× (4.384 Å Å pixel size) to a box size of 80 px,
872 and subjected to at least one round of 2D classification to eliminate obviously bad particles.
873 Next, multiple rounds of 3D classification with a 280 Å mask diameter and a regularization
874 parameter $T = 4$ were performed over many iterations to determine the proper number of discrete
875 states in a given dataset, and to ensure that particles were classified properly. Convergence of
876 classification was monitored with a custom script, *startle.py*. Several classes slightly larger than
877 the number of discrete states were used, and classes that appeared to lie along a continuous
878 conformational coordinate were subsequently re-merged into a single class. In the case of the
879 hydrolyzing dataset, SNARE substrate-bound and SNARE substrate-free particles were split into
880 separate groups of particles, re-classified, and processed independently.

881 Following classification, particles were re-centered and re-extracted with a box size of 588 px
882 and binned 2× (1.096 Å pixel size) with a box size of 294 px. Following an initial round of 3D
883 refinement and post-processing, CTF refinement was performed. Typically, defocus,
884 astigmatism, B-factor, tilt, and trefoil were refined on a per-particle or per-micrograph basis,
885 depending on the specific class. Particles were then subjected to an additional round of 3D
886 refinement and post-processing, and optimal parameters for particle polishing were determined
887 by training on several classes, yielding different parameter sets. Particle polishing was then
888 performed with these sets, and 3D refinement and post-processing were used to assess the
889 results. Polished particles were then subjected to a final round of 3D refinement, post-processing,
890 and CTF refinement, during which anisotropic magnification was estimated. At this stage,
891 particles and 3D reconstructions were imported into *CryoSPARC* for a final round of non-
892 uniform refinement, which typically improved the quality of reconstructions.

893 In the case of one class observed under hydrolyzing conditions (c4-7-16-20-24), a large degree of
894 continuous heterogeneity was observed. 3D variability analysis (3DVA) revealed a trajectory of
895 protomer F nucleotide and rebinding, so particles in the first mode were split using a custom
896 script, *split_by_3dva.py*, as current tools to do so natively were unavailable at the time. This
897 script fits a normal distribution to the eigenvector magnitude distribution and allows slicing with
898 different cutoffs. For the 3DVA subclasses (slices O and P), particles in the ±1.5 σ tails of the
899 distribution were used for reconstruction.

900 These reconstructions were considered final for the overall 20S architecture, but further
901 processing was required to generate local reconstructions of the various α-SNAP—SNARE
902 subcomplexes. In the case of the sx20S dataset, only one class was observed with ordered spire
903 density, so local refinement was relatively simple. *CryoSPARC* signal subtraction
904 (*particle_subtract*; masks generated using *Segger* 2.5.3[71] in *Chimera* 1.15[72]) was used to remove
905 the signal from NSF N, D1, and D2 domains, leaving only the α-SNAP—syntaxin H3 SNARE
906 domain tetramer subcomplex. Local refinement (*new_local_refine*) was then performed on these
907 particles with a 40º/20 Å search extent and a custom fulcrum at the N-terminal end of the
908 SNARE bundle near the point of interaction with the F protomer of the D1 ring. The resulting
909 volumes were re-centered on the center of mass (*volume_alignment_tools*), and particle
910 alignments were updated as well (*align_3D*). Then, a final round of local refinement
911 (*new_local_refine*) was performed with the map center as the fulcrum (the default setting), a
912 smaller search extent of 10º/5 Å, and a maximum alignment resolution of 0.1º. Per-particle scales
913 were also reset, and minimization was performed over a per-particle scale. This produced the
914 final reconstruction of this subcomplex for subsequent modeling. In the case of the α-SNAP—
915 2:1 and α-SNAP—2:2 binary SNARE subcomplexes, this procedure was followed for each class

916 meeting certain criteria (number of particles, ordered spire, resolution), yielding five local
917 reconstructions for the α-SNAP—2:1 binary SNARE subcomplex and six local reconstructions
918 for the α-SNAP—2:2 binary SNARE subcomplex. In each case, these reconstructions were re-
919 centered (*volume_alignment_tools*), aligned to one another with the center of mass at the origin
920 (*align_3D)*, and a final round of local refinement was run to produce a final higher-resolution
921 reconstruction incorporating data from multiple classes. This produced the final reconstruction of
922 these subcomplexes for subsequent modeling. For more details about all data sets, see Figs. S3–
923 7, Tables S1–2, and Fig. S8.

924 **Model building and refinement**

925 All manual model building and refinements were carried out using *Coot*[73]. Semi-manual
926 refinement into low-resolution features was performed with *UCSF ChimeraX*[74] and the
927 *ISOLDE*[61] plugin. Automated refinement was performed using *phenix.real_space_refine*[75,76].

928 First, models of the three α-SNAP—SNARE subcomplexes were built by rigid body fitting of
929 the best possible starting models into their corresponding densities using *UCSF ChimeraX*. In
930 each case, 3–4 copies of a high-quality α-SNAP model from the previous best 20S model (PDB
931 ID 6MDM[6]) were rigid body fit into the density. In the case of the syntaxin H3 domain tetramer
932 complex, four copies of the syntaxin chain from the high-resolution crystal structure (PDB ID
933 1N7S[49]) of the neuronal SNARE complex were docked into the density, with several
934 characteristic residues as fiducials. The quality of the local reconstructions of the SNARE—α-
935 SNAP spires allowed unique assignment of the identity of the SNARE domains, their
936 directionality, and register (Figs. 2D, 3D, 4D, Fig. S7DE, Fig. S9A). In the case of the 2:1 binary
937 SNARE complex, the syntaxin and SNAP-25 components of the same crystal structure were
938 docked into the density, but with the SNARE domain of synaptobrevin replaced with an

939 additional syntaxin H3 SNARE domain; key side chain densities as well as a distinctive kink
940 leading into the SNAP-25 SN2 domain guided placement (Fig. 3C, Fig. S9A). In the case of the
941 2:2 binary SNARE complex, a previous crystal structure (PDB ID 1JTH[34]) was docked into the
942 density without modification. In all cases, individual components were trimmed, or residues
943 were added where supported by the density. A round of *phenix.real_space_refine* was then
944 performed with only rigid-body refinement enabled for each component. Subsequent cycles of
945 manual model building were performed in *Coot* and *ISOLDE* followed by 1–7 macrocycles of
946 *phenix.real_space_refine* with global minimization and local grid search enabled. Ramachandran
947 and secondary structure restraints were used throughout.

948 Models of NSF or the different 20S supercomplexes were then built. Gold-standard models were
949 first built into two high-resolution NSF classes from a single non-hydrolyzing dataset with near-
950 atomic resolutions using the previous best model of NSF (PDB ID 6MDM[6]) as a starting model.
951 The starting model was first docked into cryo-EM density using ChimeraX. Next, a round of
952 *phenix.real_space_refine* was performed with only rigid-body refinement enabled; each large
953 and small subdomain of each protomer was treated as a single rigid body (twelve total).
954 Nucleotides and water molecules were then added where appropriate. Subsequent cycles of
955 manual model building were performed in *Coot* and *ISOLDE* followed by 1–7 macrocycles of
956 *phenix.real_space_refine* with global minimization and local grid search enabled. Ramachandran
957 and secondary structure restraints were used throughout.

958 The previously described models were then used as starting models in building the sx20S and
959 bin20S supercomplexes. In sx20S and bin20S reconstructions with well-defined N-domains (i.e.,
960 a recognizable two-lobed density), one or more instances of the re-processed model derived from
961 the crystal structure (PDB ID 1QCS[77]) as re-processed by *PDB_REDO*[78] were rigid body fit into

962 density before refinement. Next, the appropriate α-SNAP—SNARE subcomplex was docked
963 into the density, completing the spire structure. A round of *phenix.real_space_refine* was
964 performed with only rigid-body refinement enabled; each large and small subdomain of each
965 protomer, each N domain, and each α-SNAP—SNARE subcomplex was treated as a rigid body
966 (for a 20S particle with four engaged N-domains, this would be 17 total rigid body groups).
967 Nucleotides, Mg^{2+}, P_i, and water molecules were then added where appropriate. Subsequent
968 cycles of manual model building were performed in *Coot* and *ISOLDE* followed by 1–7
969 macrocycles of *phenix.real_space_refine* with global minimization and local grid search enabled.
970 Ramachandran and secondary structure restraints were used throughout.

971 All model figures were prepared with *UCSF ChimeraX*, in many cases with custom CXC scripts
972 generated by the Python scripts described below.

973 **Automated NSF model analysis and coordinate PCA**

974 Several custom Python scripts (*preprocess_models.py, analyze_models.py*) using the *Bio.PDB*
975 module[79] of the Biopython project[80] as well as *pandas*[81], *numpy*[82], *scipy*[83], *scikit-learn*[84], and
976 *matplotlib*[85] were used to standardize all 25 NSF, sx20S, or bin20S models for further analysis,
977 such as to perform principle components analysis (PCA) and HDBSCAN clustering, to measure
978 NSF D1 large-small subdomain angles, to perform planarity fits for NSF domains and
979 subdomains, to measure distances between key catalytic residues and nucleotides, and to map
980 various values to structures for visualization in *UCSF ChimeraX*.

981 For PCA, 132 NSF D1 domains from 22 models over all datasets were split into large and small
982 subdomains, which were then aligned to one another (large, residues 224–373; small, residues
983 400–486) using *Bio.PDB.Superimposer*. Splitting removes the largest source of variance in the

data, the rigid body motions of the two subdomains relative to each other, which is considered trivial for the purposes of this analysis. Next, a Cα coordinate matrix **C** with dimensions $n_{models} \times n_{residues} \times 3$ was constructed for residues shared by all models and flattened into two dimensions, creating $\mathbf{C_{flat}}$ with n_{models} rows and $n_{residues} \times 3$ columns. $\mathbf{C_{flat}}$ was then rescaled using *sklearn.preprocessing.StandardScaler* and PCA was performed on $\mathbf{C_{flat}}$ using *sklearn.decomposition.PCA*. 13 components were found to contribute 99% of the variance, so a transformed matrix $\mathbf{C_{trans}}$ with dimensions $n_{models} \times 13$, with eigenvectors sorted along the second axis by eigenvalue, was calculated. The cluster analysis of models was then performed using *sklearn.cluster.HDBSCAN* with a minimum cluster size of three, producing 11 clusters accounting for 119/132 total models. This analysis serves as the basis for Fig. 6A.

For NSF D1 and D2 plane fits, centers of mass for all subdomains were calculated, and the planes for different combinations of these points were fit using a least squares approach (Fig. S11). For NSF D1 large-small subdomain angle calculations, the primary axes of two α-helices in the large (residues 350–358) and small subdomains (residues 442–452) were calculated by singular value decomposition using *np.linalg.svd*, with implementation inspired by *helix_analysis.py* from the MDAnalysis package[86]. Vectors corresponding to these helical axes u and v were normalized and centered at the coordinate origin, and the angle between them was calculated as $\theta = 2 \times \tan^{-1}\left(\sqrt{\sum_i \vec{u}_i^2}\sqrt{\sum_i \vec{v}_i^2}\right)$.

Distances between key active site atoms over all models (Fig. S13) were calculated using *np.linalg.norm*, where the norm of the difference vector of the coordinates of each atom is the distance between them in Å. Significant changes in protomer E active site residues relative to the other five protomers were assessed by pairwise application of the Welch's t-test assuming non-

equal variances as implemented in *scipy.stats.ttest_ind*. Distance distributions were considered statistically different if $p < 0.05$.

All these values, as well as manually curated, qualitative data labels, were plotted in various ways using *matplotlib* or incorporated into automatically generated UCSF ChimeraX CXC scripts.

References

1. Rizo, J., and Südhof, T.C. (2012). The membrane fusion enigma: SNAREs, Sec1/Munc18 proteins, and their accomplices--guilty as charged? Annu. Rev. Cell Dev. Biol. *28*, 279–308. https://doi.org/10.1146/annurev-cellbio-101011-155818.

2. Brunger, A.T., Choi, U.B., Lai, Y., Leitz, J., and Zhou, Q. (2018). Molecular Mechanisms of Fast Neurotransmitter Release. Annu. Rev. Biophys. *47*, 469–497. https://doi.org/10.1146/annurev-biophys-070816-034117.

3. Leitz, J., Wang, C., Esquivies, L., Pfuetzner, R.A., Peters, J.J., Couoh-Cardel, S., Wang, A.L., and Brunger, A.T. (2024). Beyond the MUN domain, Munc13 controls priming and depriming of synaptic vesicles. Cell Rep. *43*. https://doi.org/10.1016/j.celrep.2024.114026.

4. Brunger, A.T., Choi, U.B., Lai, Y., Leitz, J., White, K.I., and Zhou, Q. (2019). The pre-synaptic fusion machinery. Curr. Opin. Struct. Biol. *54*, 179–188. https://doi.org/10.1016/j.sbi.2019.03.007.

5. Rizo, J. (2022). Molecular Mechanisms Underlying Neurotransmitter Release. Annu. Rev. Biophys. *51*, 377–408. https://doi.org/10.1146/annurev-biophys-111821-104732.

6. White, K.I., Zhao, M., Choi, U.B., Pfuetzner, R.A., and Brunger, A.T. (2018). Structural principles of SNARE complex recognition by the AAA+ protein NSF. eLife *7*, e38888. https://doi.org/10.7554/eLife.38888.

7. Zhao, M., Wu, S., Zhou, Q., Vivona, S., Cipriano, D.J., Cheng, Y., and Brunger, A.T. (2015). Mechanistic insights into the recycling machine of the SNARE complex. Nature *518*, 61–67. https://doi.org/10.1038/nature14148.

8. Rickman, C., Medine, C.N., Dun, A.R., Moulton, D.J., Mandula, O., Halemani, N.D., Rizzoli, S.O., Chamberlain, L.H., and Duncan, R.R. (2010). t-SNARE Protein Conformations Patterned by the Lipid Microenvironment. J. Biol. Chem. *285*, 13535–13541. https://doi.org/10.1074/jbc.M109.091058.

1036 9. Murray, D.H., and Tamm, L.K. (2009). Clustering of Syntaxin-1A in Model Membranes is
1037 Modulated by Phosphatidylinositol-4,5-bisphosphate and Cholesterol. Biochemistry *48*,
1038 4617–4625. https://doi.org/10.1021/bi9003217.

1039 10. Aoyagi, K., Sugaya, T., Umeda, M., Yamamoto, S., Terakawa, S., and Takahashi, M. (2005).
1040 The activation of exocytotic sites by the formation of phosphatidylinositol 4,5-bisphosphate
1041 microdomains at syntaxin clusters. J. Biol. Chem. *280*, 17346–17352.
1042 https://doi.org/10.1074/jbc.M413307200.

1043 11. Lang, T., Bruns, D., Wenzel, D., Riedel, D., Holroyd, P., Thiele, C., and Jahn, R. (2001).
1044 SNAREs are concentrated in cholesterol-dependent clusters that define docking and fusion
1045 sites for exocytosis. EMBO J. *20*, 2202–2213. https://doi.org/10.1093/emboj/20.9.2202.

1046 12. Emperador-Melero, J., and Kaeser, P.S. (2020). Assembly of the presynaptic active zone.
1047 Curr. Opin. Neurobiol. *63*, 95–103. https://doi.org/10.1016/j.conb.2020.03.008.

1048 13. Weimbs, T., Low, S.H., Chapin, S.J., Mostov, K.E., Bucher, P., and Hofmann, K. (1997). A
1049 conserved domain is present in different families of vesicular fusion proteins:
1050 A new superfamily. Proc. Natl. Acad. Sci. U. S. A. *94*, 3046–3051.

1051 14. Bennett, M.K., Calakos, N., and Scheller, R.H. (1992). Syntaxin: A Synaptic Protein
1052 Implicated in Docking of Synaptic Vesicles at Presynaptic Active Zones. Science *257*, 255–
1053 259. https://doi.org/10.1126/science.1321498.

1054 15. Sutton, R.B., Fasshauer, D., Jahn, R., and Brunger, A.T. (1998). Crystal structure of a
1055 SNARE complex involved in synaptic exocytosis at 2.4 Å resolution. Nature *395*, 347–353.
1056 https://doi.org/10.1038/26412.

1057 16. Fernandez, I., Ubach, J., Dulubova, I., Zhang, X., Südhof, T.C., and Rizo, J. (1998). Three-
1058 Dimensional Structure of an Evolutionarily Conserved N-Terminal Domain of Syntaxin 1A.
1059 Cell *94*, 841–849. https://doi.org/10.1016/s0092-8674(00)81742-0.

1060 17. Sieber, J.J., Willig, K.I., Kutzner, C., Gerding-Reimers, C., Harke, B., Donnert, G.,
1061 Rammner, B., Eggeling, C., Hell, S.W., Grubmüller, H., et al. (2007). Anatomy and
1062 Dynamics of a Supramolecular Membrane Protein Cluster. Science *317*, 1072–1076.
1063 https://doi.org/10.1126/science.1141727.

1064 18. Bar-On, D., Wolter, S., Van De Linde, S., Heilemann, M., Nudelman, G., Nachliel, E.,
1065 Gutman, M., Sauer, M., and Ashery, U. (2012). Super-resolution Imaging Reveals the
1066 Internal Architecture of Nano-sized Syntaxin Clusters. J. Biol. Chem. *287*, 27158–27167.
1067 https://doi.org/10.1074/jbc.M112.353250.

1068 19. Knowles, M.K., Barg, S., Wan, L., Midorikawa, M., Chen, X., and Almers, W. (2010). Single
1069 secretory granules of live cells recruit syntaxin-1 and synaptosomal associated protein 25
1070 (SNAP-25) in large copy numbers. Proc. Natl. Acad. Sci. *107*, 20810–20815.
1071 https://doi.org/10.1073/pnas.1014840107.

1072 20. Wan, L., Chen, X., and Almers, W. (2021). Munc18-dependent and -independent clustering
1073 of syntaxin in the plasma membrane of cultured endocrine cells. Proc. Natl. Acad. Sci. *118*,
1074 e2025748118. https://doi.org/10.1073/pnas.2025748118.

1075 21. Ullrich, A., Böhme, M.A., Schöneberg, J., Depner, H., Sigrist, S.J., and Noé, F. (2015).
1076 Dynamical Organization of Syntaxin-1A at the Presynaptic Active Zone. PLOS Comput.
1077 Biol. *11*, e1004407. https://doi.org/10.1371/journal.pcbi.1004407.

1078 22. Barg, S., Knowles, M.K., Chen, X., Midorikawa, M., and Almers, W. (2010). Syntaxin
1079 clusters assemble reversibly at sites of secretory granules in live cells. Proc. Natl. Acad. Sci.
1080 *107*, 20804–20809. https://doi.org/10.1073/pnas.1014823107.

1081 23. Sakamoto, H., Ariyoshi, T., Kimpara, N., Sugao, K., Taiko, I., Takikawa, K., Asanuma, D.,
1082 Namiki, S., and Hirose, K. (2018). Synaptic weight set by Munc13-1 supramolecular
1083 assemblies. Nat. Neurosci. *21*, 41–49. https://doi.org/10.1038/s41593-017-0041-9.

1084 24. Pertsinidis, A., Mukherjee, K., Sharma, M., Pang, Z.P., Park, S.R., Zhang, Y., Brunger, A.T.,
1085 Südhof, T.C., and Chu, S. (2013). Ultrahigh-resolution imaging reveals formation of
1086 neuronal SNARE/Munc18 complexes in situ. Proc. Natl. Acad. Sci. *110*, E2812–E2820.
1087 https://doi.org/10.1073/pnas.1310654110.

1088 25. Yin, P., Gandasi, N.R., Arora, S., Omar-Hmeadi, M., Saras, J., and Barg, S. (2018). Syntaxin
1089 clusters at secretory granules in a munc18-bound conformation. Mol. Biol. Cell *29*, 2700–
1090 2708. https://doi.org/10.1091/mbc.E17-09-0541.

1091 26. Lang, T. (2007). SNARE proteins and 'membrane rafts.' J. Physiol. *585*, 693–698.
1092 https://doi.org/10.1113/jphysiol.2007.134346.

1093 27. Bademosi, A.T., Lauwers, E., Padmanabhan, P., Odierna, L., Chai, Y.J., Papadopulos, A.,
1094 Goodhill, G.J., Verstreken, P., van Swinderen, B., and Meunier, F.A. (2016). In vivo single-
1095 molecule imaging of syntaxin1A reveals polyphosphoinositide- and activity-dependent
1096 trapping in presynaptic nanoclusters. Nat. Commun. *7*, 13660.
1097 https://doi.org/10.1038/ncomms13660.

1098 28. Sieber, J.J., Willig, K.I., Heintzmann, R., Hell, S.W., and Lang, T. (2006). The SNARE Motif
1099 Is Essential for the Formation of Syntaxin Clusters in the Plasma Membrane. Biophys. J. *90*,
1100 2843–2851. https://doi.org/10.1529/biophysj.105.079574.

1101 29. Hanson, P.I., Otto, H., Barton, N., and Jahn, R. (1995). The N-Ethylmaleimide-sensitive
1102 Fusion Protein and α-SNAP Induce a Conformational Change in Syntaxin (*). J. Biol. Chem.
1103 *270*, 16955–16961. https://doi.org/10.1074/jbc.270.28.16955.

1104 30. Stepien, K.P., Prinslow, E.A., and Rizo, J. (2019). Munc18-1 is crucial to overcome the
1105 inhibition of synaptic vesicle fusion by αSNAP. Nat. Commun. *10*, 4326.
1106 https://doi.org/10.1038/s41467-019-12188-4.

1107 31. Ma, C., Su, L., Seven, A.B., Xu, Y., and Rizo, J. (2013). Reconstitution of the vital functions
1108 of Munc18 and Munc13 in neurotransmitter release. Science *339*, 421–425.
1109 https://doi.org/10.1126/science.1230473.

1110 32. Choi, U.B., Zhao, M., White, K.I., Pfuetzner, R.A., Esquivies, L., Zhou, Q., and Brunger,
1111 A.T. (2018). NSF-mediated disassembly of on- and off-pathway SNARE complexes and
1112 inhibition by complexin. eLife *7*, e36497. https://doi.org/10.7554/eLife.36497.

1113 33. Fasshauer, D., Bruns, D., Shen, B., Jahn, R., and Brunger, A.T. (1997). A Structural Change
1114 Occurs upon Binding of Syntaxin to SNAP-25. J. Biol. Chem. *272*, 4582–4590.
1115 https://doi.org/10.1074/jbc.272.7.4582.

1116 34. Misura, K.M.S., Gonzalez, L.C., May, A.P., Scheller, R.H., and Weis, W.I. (2001). Crystal
1117 Structure and Biophysical Properties of a Complex between the N-terminal SNARE Region
1118 of SNAP25 and Syntaxin 1a *. J. Biol. Chem. *276*, 41301–41309.
1119 https://doi.org/10.1074/jbc.M106853200.

1120 35. Weninger, K., Bowen, M.E., Choi, U.B., Chu, S., and Brunger, A.T. (2008). Accessory
1121 Proteins Stabilize the Acceptor Complex for Synaptobrevin, the 1:1 Syntaxin/SNAP-25
1122 Complex. Structure *16*, 308–320. https://doi.org/10.1016/j.str.2007.12.010.

1123 36. Hesselbarth, J., and Schmidt, C. (2023). Mass spectrometry uncovers intermediates and off-
1124 pathway complexes for SNARE complex assembly. Commun. Biol. *6*, 1–15.
1125 https://doi.org/10.1038/s42003-023-04548-0.

1126 37. Hayashi, T., McMahon, H., Yamasaki, S., Binz, T., Hata, Y., Südhof, T.C., and Niemann, H.
1127 (1994). Synaptic vesicle membrane fusion complex: action of clostridial neurotoxins on
1128 assembly. EMBO J. *13*, 5051–5061. https://doi.org/10.1002/j.1460-2075.1994.tb06834.x.

1129 38. Gao, Y., Khan, Y.A., Mo, W., White, K.I., Perkins, M., Pfuetzner, R.A., Trapani, J.G.,
1130 Brunger, A.T., and Nicolson, T. (2023). Sensory deficit screen identifies nsf mutation that
1131 differentially affects SNARE recycling and quality control. Cell Rep. *42*.
1132 https://doi.org/10.1016/j.celrep.2023.112345.

1133 39. Hayashi, T., Yamasaki, S., Nauenburg, S., Binz, T., and Niemann, H. (1995). Disassembly of
1134 the reconstituted synaptic vesicle membrane fusion complex in vitro. EMBO J. *14*, 2317–
1135 2325. https://doi.org/10.1002/j.1460-2075.1995.tb07226.x.

1136 40. Vivona, S., Cipriano, D.J., O'Leary, S., Li, Y.H., Fenn, T.D., and Brunger, A.T. (2013).
1137 Disassembly of All SNARE Complexes by N-Ethylmaleimide-sensitive Factor (NSF) Is
1138 Initiated by a Conserved 1:1 Interaction between α-Soluble NSF Attachment Protein (SNAP)
1139 and SNARE Complex. J. Biol. Chem. *288*, 24984–24991.
1140 https://doi.org/10.1074/jbc.M113.489807.

1141 41. Zhao, M., Wu, S., Zhou, Q., Vivona, S., Cipriano, D.J., Cheng, Y., and Brunger, A.T. (2015).
1142 Mechanistic insights into the recycling machine of the SNARE complex. Nature *518*, 61–67.
1143 https://doi.org/10.1038/nature14148.

1144 42. Nagiec, E.E., Bernstein, A., and Whiteheart, S.W. (1995). Each Domain of the N-
1145 Ethylmaleimide-sensitive Fusion Protein Contributes to Its Transport Activity (*). J. Biol.
1146 Chem. *270*, 29182–29188. https://doi.org/10.1074/jbc.270.49.29182.

1147 43. Matveeva, E.A., He, P., and Whiteheart, S.W. (1997). N-Ethylmaleimide-sensitive Fusion
1148 Protein Contains High and Low Affinity ATP-binding Sites That Are Functionally Distinct *.
1149 J. Biol. Chem. *272*, 26413–26418. https://doi.org/10.1074/jbc.272.42.26413.

1150 44. Xiao, W., Poirier, M.A., Bennett, M.K., and Shin, Y.-K. (2001). The neuronal t-SNARE
1151 complex is a parallel four-helix bundle. Nat. Struct. Biol. *8*, 308–311.
1152 https://doi.org/10.1038/86174.

1153 45. Margittai, M., Fasshauer, D., Pabst, S., Jahn, R., and Langen, R. (2001). Homo- and
1154 Heterooligomeric SNARE Complexes Studied by Site-directed Spin Labeling *. J. Biol.
1155 Chem. *276*, 13169–13177. https://doi.org/10.1074/jbc.M010653200.

1156 46. Lai, Y., Choi, U.B., Leitz, J., Rhee, H.J., Lee, C., Altas, B., Zhao, M., Pfuetzner, R.A., Wang,
1157 A.L., Brose, N., et al. (2017). Molecular Mechanisms of Synaptic Vesicle Priming by
1158 Munc13 and Munc18. Neuron *95*, 591-607.e10.
1159 https://doi.org/10.1016/j.neuron.2017.07.004.

1160 47. Stepien, K.P., Xu, J., Zhang, X., Bai, X.-C., and Rizo, J. (2022). SNARE assembly
1161 enlightened by cryo-EM structures of a synaptobrevin–Munc18-1–syntaxin-1 complex. Sci.
1162 Adv. *8*, eabo5272. https://doi.org/10.1126/sciadv.abo5272.

1163 48. Sanyal, S., and Krishnan, K.S. (2001). Lethal comatose mutation in Drosophila reveals
1164 possible role for NSF in neurogenesis. NeuroReport *12*, 1363.

1165 49. Ernst, J.A., and Brunger, A.T. (2003). High Resolution Structure, Stability, and
1166 Synaptotagmin Binding of a Truncated Neuronal SNARE Complex *. J. Biol. Chem. *278*,
1167 8630–8636. https://doi.org/10.1074/jbc.M211889200.

1168 50. de la Peña, A.H., Goodall, E.A., Gates, S.N., Lander, G.C., and Martin, A. (2018). Substrate-
1169 engaged 26S proteasome structures reveal mechanisms for ATP-hydrolysis–driven
1170 translocation. Science *362*, eaav0725. https://doi.org/10.1126/science.aav0725.

1171 51. Punjani, A., and Fleet, D.J. (2021). 3D variability analysis: Resolving continuous flexibility
1172 and discrete heterogeneity from single particle cryo-EM. J. Struct. Biol. *213*, 107702.
1173 https://doi.org/10.1016/j.jsb.2021.107702.

1174 52. Khan, Y.A., White, K.I., Pfuetzner, R.A., Singal, B., Esquivies, L., Mckenzie, G., Liu, F.,
1175 DeLong, K., Choi, U.B., Montabana, E., et al. (2024). Sec18 side-loading is essential for
1176 universal SNARE recycling across cellular contexts. Preprint at bioRxiv,
1177 https://doi.org/10.1101/2024.08.30.610324 https://doi.org/10.1101/2024.08.30.610324.

1178 53. Zhou, H., Di Palma, S., Preisinger, C., Peng, M., Polat, A.N., Heck, A.J.R., and Mohammed,
1179 S. (2013). Toward a Comprehensive Characterization of a Human Cancer Cell
1180 Phosphoproteome. J. Proteome Res. *12*, 260–271. https://doi.org/10.1021/pr300630k.

1181 54. Zhou, Q., Zhou, P., Wang, A.L., Wu, D., Zhao, M., Südhof, T.C., and Brunger, A.T. (2017).
1182 The primed SNARE–complexin–synaptotagmin complex for neuronal exocytosis. Nature
1183 *548*, 420–425. https://doi.org/10.1038/nature23484.

1184 55. Zhou, Q., Lai, Y., Bacaj, T., Zhao, M., Lyubimov, A.Y., Uervirojnangkoorn, M., Zeldin, O.B.,
1185 Brewster, A.S., Sauter, N.K., Cohen, A.E., et al. (2015). Architecture of the synaptotagmin–
1186 SNARE machinery for neuronal exocytosis. Nature *525*, 62–67.
1187 https://doi.org/10.1038/nature14975.

1188 56. Smith, G.R., Contreras-Moreira, B., Zhang, X., and Bates, P.A. (2004). A link between
1189 sequence conservation and domain motion within the AAA+ family. J. Struct. Biol. *146*,
1190 189–204. https://doi.org/10.1016/j.jsb.2003.11.022.

1191 57. Khan, Y.A., White, K.I., and Brunger, A.T. (2022). The AAA+ superfamily: a review of the
1192 structural and mechanistic principles of these molecular machines. Crit. Rev. Biochem. Mol.
1193 Biol. *57*, 156–187. https://doi.org/10.1080/10409238.2021.1979460.

1194 58. Huang, X., Sun, S., Wang, X., Fan, F., Zhou, Q., Lu, S., Cao, Y., Wang, Q.-W., Dong, M.-Q.,
1195 Yao, J., et al. (2019). Mechanistic insights into the SNARE complex disassembly. Sci. Adv.
1196 *5*, eaau8164. https://doi.org/10.1126/sciadv.aau8164.

1197 59. Greaves, J., Gorleku, O.A., Salaun, C., and Chamberlain, L.H. (2010). Palmitoylation of the
1198 SNAP25 Protein Family. J. Biol. Chem. *285*, 24629–24638.
1199 https://doi.org/10.1074/jbc.M110.119289.

1200 60. Jumper, J., Evans, R., Pritzel, A., Green, T., Figurnov, M., Ronneberger, O.,
1201 Tunyasuvunakool, K., Bates, R., Žídek, A., Potapenko, A., et al. (2021). Highly accurate
1202 protein structure prediction with AlphaFold. Nature *596*, 583–589.
1203 https://doi.org/10.1038/s41586-021-03819-2.

1204 61. Croll, T.I. (2018). ISOLDE: a physically realistic environment for model building into low-
1205 resolution electron-density maps. Acta Crystallogr. Sect. Struct. Biol. *74*, 519–530.
1206 https://doi.org/10.1107/S2059798318002425.

1207 62. Schneider, C.A., Rasband, W.S., and Eliceiri, K.W. (2012). NIH Image to ImageJ: 25 years
1208 of image analysis. Nat. Methods *9*, 671–675. https://doi.org/10.1038/nmeth.2089.

1209 63. Cipriano, D.J., Jung, J., Vivona, S., Fenn, T.D., Brunger, A.T., and Bryant, Z. (2013).
1210 Processive ATP-driven Substrate Disassembly by the N-Ethylmaleimide-sensitive Factor
1211 (NSF) Molecular Machine♦. J. Biol. Chem. *288*, 23436–23445.
1212 https://doi.org/10.1074/jbc.M113.476705.

1213 64. Studier, F.W. (2005). Protein production by auto-induction in high-density shaking cultures.
1214 Protein Expr. Purif. *41*, 207–234. https://doi.org/10.1016/j.pep.2005.01.016.

1215 65. Mastronarde, D.N. (2005). Automated electron microscope tomography using robust
1216 prediction of specimen movements. J. Struct. Biol. *152*, 36–51.
1217 https://doi.org/10.1016/j.jsb.2005.07.007.

66. Zheng, S.Q., Palovcak, E., Armache, J.-P., Verba, K.A., Cheng, Y., and Agard, D.A. (2017). MotionCor2 - anisotropic correction of beam-induced motion for improved cryo-electron microscopy. Nat. Methods *14*, 331–332. https://doi.org/10.1038/nmeth.4193.

67. Rohou, A., and Grigorieff, N. (2015). CTFFIND4: Fast and accurate defocus estimation from electron micrographs. J. Struct. Biol. *192*, 216–221. https://doi.org/10.1016/j.jsb.2015.08.008.

68. Scheres, S.H.W. (2012). RELION: Implementation of a Bayesian approach to cryo-EM structure determination. J. Struct. Biol. *180*, 519–530. https://doi.org/10.1016/j.jsb.2012.09.006.

69. Zivanov, J., Nakane, T., Forsberg, B.O., Kimanius, D., Hagen, W.J., Lindahl, E., and Scheres, S.H. (2018). New tools for automated high-resolution cryo-EM structure determination in RELION-3. eLife *7*, e42166. https://doi.org/10.7554/eLife.42166.

70. Punjani, A., Rubinstein, J.L., Fleet, D.J., and Brubaker, M.A. (2017). cryoSPARC: algorithms for rapid unsupervised cryo-EM structure determination. Nat. Methods *14*, 290–296. https://doi.org/10.1038/nmeth.4169.

71. Pintilie, G.D., Zhang, J., Goddard, T.D., Chiu, W., and Gossard, D.C. (2010). Quantitative analysis of cryo-EM density map segmentation by watershed and scale-space filtering, and fitting of structures by alignment to regions. J. Struct. Biol. *170*, 427–438. https://doi.org/10.1016/j.jsb.2010.03.007.

72. Pettersen, E.F., Goddard, T.D., Huang, C.C., Couch, G.S., Greenblatt, D.M., Meng, E.C., and Ferrin, T.E. (2004). UCSF Chimera—A visualization system for exploratory research and analysis. J. Comput. Chem. *25*, 1605–1612. https://doi.org/10.1002/jcc.20084.

73. Emsley, P., Lohkamp, B., Scott, W.G., and Cowtan, K. (2010). Features and development of Coot. Acta Crystallogr. D Biol. Crystallogr. *66*, 486–501. https://doi.org/10.1107/S0907444910007493.

74. Goddard, T.D., Huang, C.C., Meng, E.C., Pettersen, E.F., Couch, G.S., Morris, J.H., and Ferrin, T.E. (2018). UCSF ChimeraX: Meeting modern challenges in visualization and analysis. Protein Sci. *27*, 14–25. https://doi.org/10.1002/pro.3235.

75. Adams, P.D., Afonine, P.V., Bunkóczi, G., Chen, V.B., Davis, I.W., Echols, N., Headd, J.J., Hung, L.-W., Kapral, G.J., Grosse-Kunstleve, R.W., et al. (2010). PHENIX: a comprehensive Python-based system for macromolecular structure solution. Acta Crystallogr. D Biol. Crystallogr. *66*, 213–221. https://doi.org/10.1107/S0907444909052925.

76. Afonine, P.V., Poon, B.K., Read, R.J., Sobolev, O.V., Terwilliger, T.C., Urzhumtsev, A., and Adams, P.D. (2018). Real-space refinement in PHENIX for cryo-EM and crystallography. Acta Crystallogr. Sect. Struct. Biol. *74*, 531–544. https://doi.org/10.1107/S2059798318006551.

77. Yu, R.C., Jahn, R., and Brunger, A.T. (1999). NSF N-Terminal Domain Crystal Structure: Models of NSF Function. Mol. Cell *4*, 97–107. https://doi.org/10.1016/S1097-2765(00)80191-4.

78. Joosten, R.P., Long, F., Murshudov, G.N., and Perrakis, A. (2014). The PDB_REDO server for macromolecular structure model optimization. IUCrJ *1*, 213–220. https://doi.org/10.1107/S2052252514009324.

79. Hamelryck, T., and Manderick, B. (2003). PDB file parser and structure class implemented in Python. Bioinformatics *19*, 2308–2310. https://doi.org/10.1093/bioinformatics/btg299.

80. Cock, P.J.A., Antao, T., Chang, J.T., Chapman, B.A., Cox, C.J., Dalke, A., Friedberg, I., Hamelryck, T., Kauff, F., Wilczynski, B., et al. (2009). Biopython: freely available Python tools for computational molecular biology and bioinformatics. Bioinformatics *25*, 1422–1423. https://doi.org/10.1093/bioinformatics/btp163.

81. McKinney, W. (2010). Data Structures for Statistical Computing in Python. In Proceedings of the 9th Python in Science Confference, pp. 56–61. https://doi.org/10.25080/Majora-92bf1922-00a.

82. Harris, C.R., Millman, K.J., van der Walt, S.J., Gommers, R., Virtanen, P., Cournapeau, D., Wieser, E., Taylor, J., Berg, S., Smith, N.J., et al. (2020). Array programming with NumPy. Nature *585*, 357–362. https://doi.org/10.1038/s41586-020-2649-2.

83. Virtanen, P., Gommers, R., Oliphant, T.E., Haberland, M., Reddy, T., Cournapeau, D., Burovski, E., Peterson, P., Weckesser, W., Bright, J., et al. (2020). SciPy 1.0: fundamental algorithms for scientific computing in Python. Nat. Methods *17*, 261–272. https://doi.org/10.1038/s41592-019-0686-2.

84. Pedregosa, F., Varoquaux, G., Gramfort, A., Michel, V., Thirion, B., Grisel, O., Blondel, M., Prettenhofer, P., Weiss, R., Dubourg, V., et al. (2011). Scikit-learn: Machine Learning in Python. J. Mach. Learn. Res. *12*, 2825–2830.

85. Hunter, J.D. (2007). Matplotlib: A 2D Graphics Environment. Comput. Sci. Eng. *9*, 90–95. https://doi.org/10.1109/MCSE.2007.55.

86. Gowers, R.J., Linke, M., Barnoud, J., Reddy, T.J.E., Melo, M.N., Seyler, S.L., DomaÅ„ski, J., Dotson, D.L., Buchoux, S., Kenney, I.M., et al. (2016). MDAnalysis: A Python Package for the Rapid Analysis of Molecular Dynamics Simulations. In Proceedings of the 15th Python in Science Conference, S. Benthall and S. Rostrup, eds., pp. 98–105. https://doi.org/10.25080/Majora-629e541a-00e.